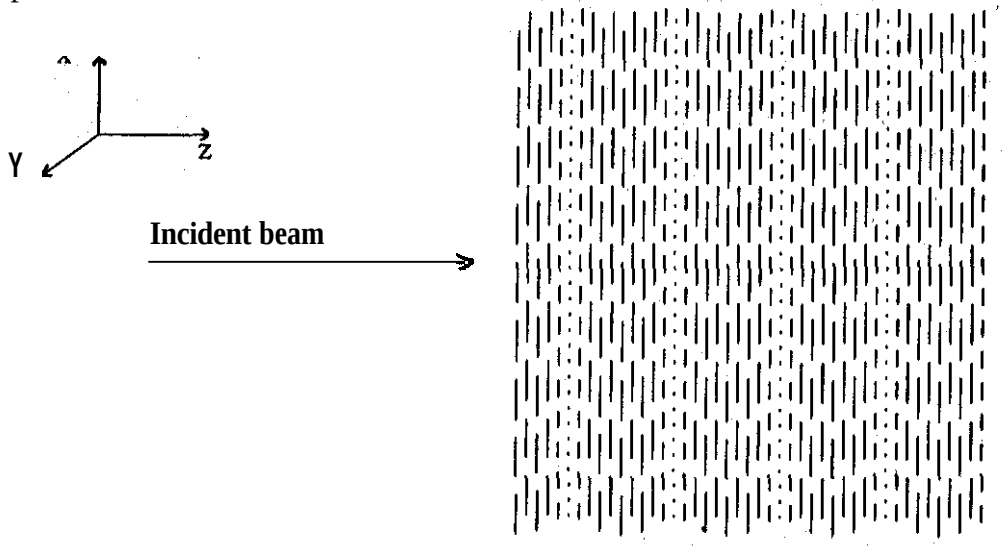

Fig 6.1: Geometry for Bragg reflection

the Bragg regime is shown in Fig 6.1. In the case of a plane monochromatic wave incident on the medium at z=0, only four out of the six components of the E,H arc independent. We choose the these independent components lo be the x and y components of E *i.e.,* (Ex, Ey) and H *i.e.,* **(I-lx,** Hy). Then the Maxwell's equations take the form:

$$\frac{d\Psi(z)}{dz} = jkD(z)\Psi(z) \tag{6.1}$$

where.

$k = \omega/c$

$$\Psi = \begin{bmatrix} E_x \\ H_y \\ E_y \\ -H_x \end{bmatrix} = \left[E_x,\ H_y,\ E_y\ -H_x \right]^t$$

$D(z)$ is a differential propagation matrix given by:

$$\begin{bmatrix} 0 & 1 - X^2/\epsilon_3 & 0 & 0 \\ \epsilon + \delta\cos 2qz & 0 & 6\sin 2qt & 0 \\ 0 & 0 & 0 & 1 \\ 6\sin 2qz & 0 & \epsilon - X^2 - \delta\cos 2qz & 0 \end{bmatrix}$$

here

$A = (2\pi/\lambda)\sqrt{\epsilon_0}\sin\theta_i$

θ_i = angle of incidence with respect to the pitch

ϵ_0 = dielectric constant of the incident medium
λ = wavelength of light
$\epsilon = (\epsilon_1 + \epsilon_2)/2$
$\delta = (\epsilon_1 - \epsilon_2)/2$
$q = 2\pi/P$
P = pitch

ϵ_1, ϵ_2, ϵ_3 are the principle values of the dielectric ellipsoid with ϵ_3 along the z axis

Integrating (6.1) over one period gives

$$\Psi(z) = F(0,z)\Psi(0) \tag{6.2}$$

where F is a 4 x 4 transfer matrix. The eigen vectors of the matrix F gives the net electromagnetic field for the proper modes. In the reflection band these modes correspond to the waves formed by the superposition of the waves propagating along the forward and backward directions. The electromagnetic field vector components at any arbitrary location (nP+h) (for any integer n and $0 < h < P$) is determined by multiplying the eigen vector of F(0,nP) by F(nP,h). Using this method we can study the polarization structure of the eigen waves.

In an experimental situation the sample is usually confined between two homogeneous transparent isotropic media. To analyze such cases we express the Berreman vector $\Psi(z)$ as a superposition of the waves in the confining media through a transformation [4]

$$\Psi = B\Phi$$

Here B is a 4 x 4 matrix with columns representing the proper modes in the isotropic media (the eigenvcctors of D(isotropic)) and $\Phi = \begin{bmatrix} t_e & t_m & r_e & r_m \end{bmatrix}^t$ with t_e, t_m representing the complex amplitudes of Ex, Ey modes propagating in the $+z$ direction and r_e, r_m are the corresponding strengths in the $-z$ direction.

Thus when $\begin{bmatrix} i1 & i2 \end{bmatrix}$, $\begin{bmatrix} r1 & r2 \end{bmatrix}$ and $\begin{bmatrix} t1 & t2 \end{bmatrix}$ are the strengths of the incident, reflected and transmitted Ex and Ey modes respectively, equation (6.2) can be writlen as

$$\begin{bmatrix} i1 \\ i2 \\ r1 \\ r2 \end{bmatrix} = G \begin{bmatrix} t1 \\ t2 \\ 0 \\ 0 \end{bmatrix} \tag{6.3}$$

where $G = B^{-1}F^{-1}B$. From equation (6.3) we obtain 2×2 transmission matrix T and reflection matrix R to be such that:

$$\begin{bmatrix} t1 \\ t2 \end{bmatrix} = T \begin{bmatrix} i1 \\ i2 \end{bmatrix}$$

and

$$\begin{bmatrix} r1 \\ r2 \end{bmatrix} = R \begin{bmatrix} i1 \\ i2 \end{bmatrix}$$

The eigenvectors Γ of the matrix G give the proper modes of the multilayer in terms of the modes in the bounding isotropic media. This allows us to analyze the attenuated waves in the reflection band in terms of the forward and backward propagating waves. For example in the case of normal cholesterics we see that a standing wave is formed by the right and left circular waves propagating in the $+z$ and $-z$ directions. Thus, in this case we have, $\Gamma(1) = j\Gamma(2)$ and $\Gamma(3) = -j\Gamma(4)$.

It should also be mentioned that the vector $\Psi(P)$ is linearly related to $\Psi(0)$ through the Berreman matrix F. We also see that

$$\Psi(P)^t S \Psi(P) = \Psi(0)^t S \Psi(0) = 0 \tag{6.4}$$

where

$$S = \begin{bmatrix} 0 & 1 & 0 & 0 \\ -1 & 0 & 0 & 0 \\ 0 & 0 & 0 & 1 \\ 0 & 0 & -1 & 0 \end{bmatrix}$$

since

$$F(0, P)\Psi(0) = \Psi(P)$$

we get from 6.4

$$\Psi(0)^t F^t S F \Psi(0) = \Psi(0)^t S \Psi(0)$$

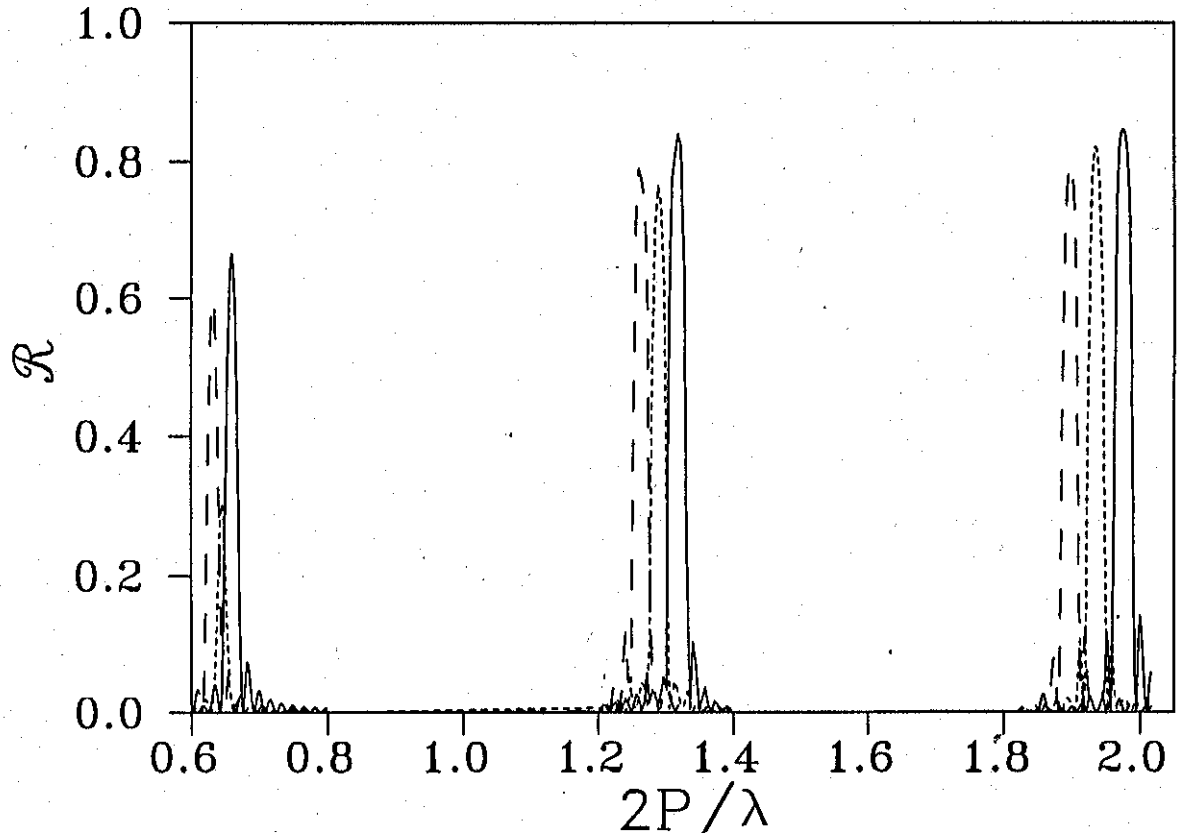

Fig **6.2:** The first three orders in the reflection spectra of a cholesteric π soliton lattice for normal incidence at H = **22065** Gauss, and $\chi_a = \mathbf{10^{-6}}$. Contineous line is the $(E_y - E_y)$ reflection. Broken line represents the $(E_x - E_x)$ reflection. The $(E_x - E_y)$ and $(E_y - E_x)$ reflections are represented by the doted line. $n_e = 1.595$, and $n_o = 1.505$.

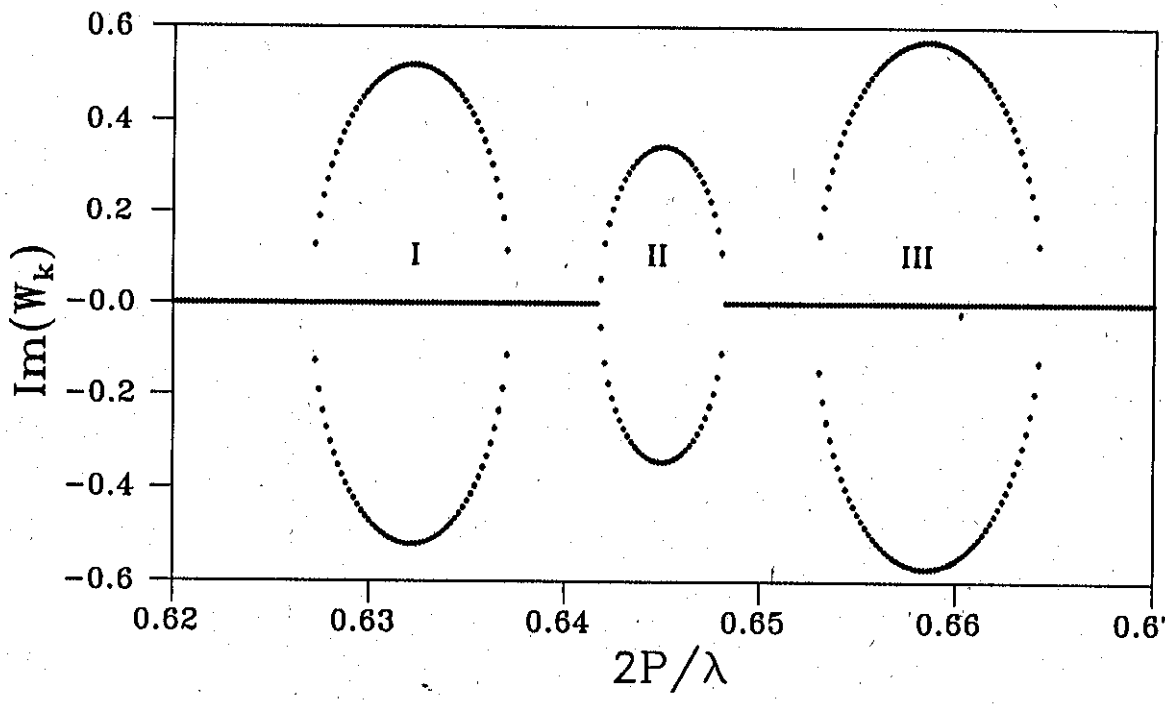

Fig **6.3:** The imaginary part of the wavevector W_k in the first reflection band of the π soliton lattice.

or

$$F^t S F = S \tag{6.5}$$

Equation, 6.5 shows that the matrix F(0,P) is symplectic [10]. Then from the properties of symplectic matrices we get that if A is an eigen value then so are A*, $1/\lambda$ and $1/\lambda^*$. Where A* is the complex conjugate of λ. This property of the simplectic matrices results in the coupling of the eigenvalues. For example far away from the refiection band we have all the Xs complex with $\lambda\lambda^* = 1$. Here we have only two independent eigenvalues. Let this be λ_1 and λ_2 then the other two are fixed as $\lambda_1^* = 1/\lambda_1$ and $\lambda_2^* = 1/\lambda_2$. In the Bragg band we have two real eigenvalues with one being the inverse of the other. The other two eigenvalues are complex with unit modules and are complex conjugates of each other. On the other hand in the non-Bragg band we have complex eigenvalues with the modules not equal to one. Thus here all the eigenvalues are coupled and are given as $(\lambda_1, 1/\lambda_1, \lambda_1^*, 1/\lambda_1^*)$. Therefore, in the non-Bragg regions there cannot be any propagating modes since the medium is non absorbing.

Using matrices R and T we can compute the reflection and transmission spectra of the soliton lattices. As mentioned earlier the soliton lattice exhibits multiple reflection bands. In addition we find that when the applied field is close to the cholesteric-nematic transition field H_{Ch-N} some of the higher orders are more intense than the first order. In Fig 6.2, we show the reflection spectra of a π soliton lattice. It should be remarked that each Bragg reflection peak of a normal cholesteric splits here into three peaks.

In Fig 6.3 we show, the computed dispersion curve in the first reflection band of the same π soliton lattice. It has three sub-bands. The eigen modes of the transmission matrix T are linear in all the three regions. For regions I and III we have a propagating mode and an attenuated mode. The attenuated mode experiences reflection and the net vibration at any point is obtained by adding the forward and backward propagation waves of the same polarization (The eigen vectors of the matrix F gives this net vibrations). For these standing vibrations E is perpendicular to H with a relative phase of $\pi/2$ between them. The propagating modes in I and III are orthogonal to each other. The same is true for attenuated modes also. This is clearly sekn in the reflection spectra given in Fig 6.2, where the side lobes df each reflection band has orthogonal polarization states. In region II we have non-Bragg

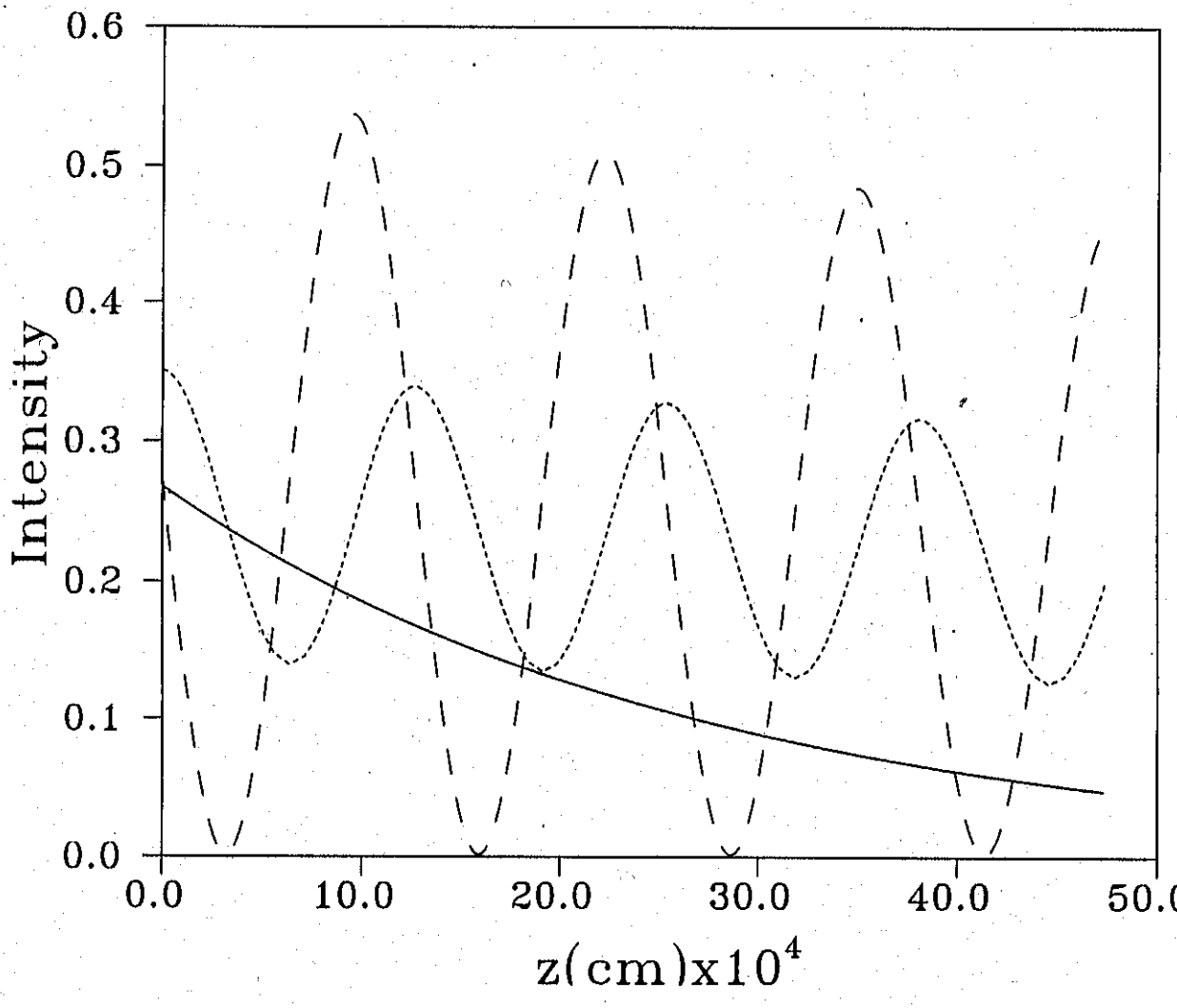

Fig **6.4:** The variation of $|E^2|$ with z of the attenuated modes in regions corresponding to I and III (broken line) and in region II (doted line). The same in the reflection band of normal cholesteric (continuous line) is given for comparison.

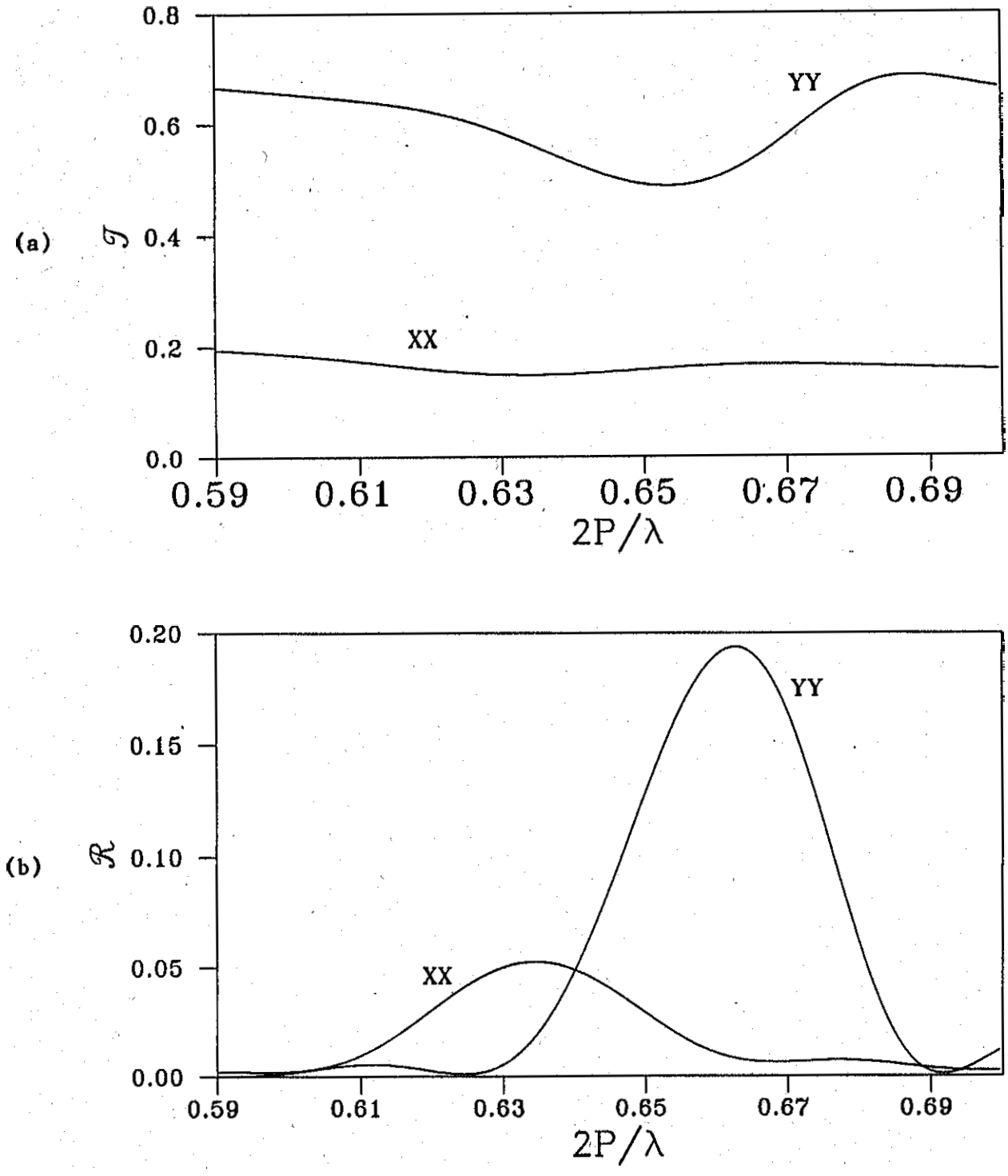

Fig 6.5: The transmission coefficient $\mathcal{T}$ (a) and reflection coefficient $\mathcal{R}$ (b) of a π soliton lattice in the presence of linear dichroism. $n_e = 1.595 + .025j$, $n_e = 1.805 + .001j$, other parameters being the same as Figure:6.2

reflection where both eigen modes are attenuated. Thus for any forward propagating wave there is a wave going in the opposite direction, which is interestingly is of orthogonal polarization. Because of this reason the reflected light here will always have the polarization orthogonal to that of the incident wave. This is shown in Fig 6.2. The net wave in this region (which is a superposition of the forward and backward propagating waves of orthogonal polarizations) is elliptical with its ellipticity varying along the twist axis.

By contrast, in the reflection band of a normal cholesteric the net attenuated mode is locally linear and is coupled to the local director. The E and H vectors of this mode are parallel to each other with a phase difference of $\pi/2$ between them.

In Fig 6.4, we give the variation of $|E|^2$ as a function z of these attenuated modes in the soliton lattices and the usual cholesteric.

The reflection and transmission spectra of cliolesteric soliton lattices get altered considerably when we include linear dichroism. This is shown in Fig 6.5 for two incident linear polarizations. It should be noticed that on the shorter wave length side, the Ey mode (marked YY) is found to be strongly reflected as well as transmitted compared to the Ex mode (marked XX). Also we get, an anomalous transmission compared to the medium with avcragc refractive index.

The optical properties of cholesteric soliton lattices are in many ways similar to that of cholesterics at oblique incidence [8]. Many of it's features like the multiple Bragg reflection, the splitting of Bragg bands, and the anomalous transmission can be seen here also [9].

6.3 Phase grating mode

All the interesting results of the previous section are rather difficult to realise in practice. This is due to the large period of these lattices; On the other hand this large period of the soliton lattices makes them more suitable to be studied in the phase grating mode. In fact in this mode we require periods of the grating to be large compare to the wave length of light. Here the direction of incidence is perpendicular to the twist axis. In this geometry an incident plane wavefront emrges as a corrugated wavefront. This is shown in Fig 6.6. Raman and Nath [RN] in 1935 [10] developed a theory of isotropic gratings with phase modulation. This theory

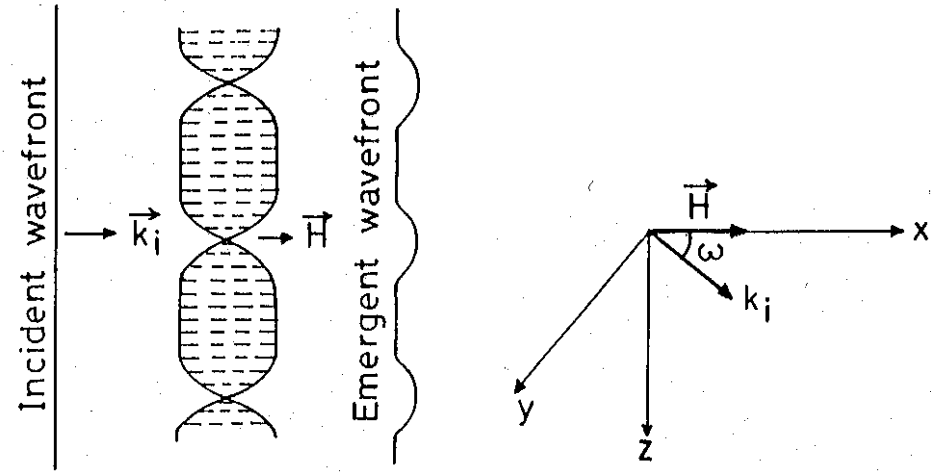

Fig 6.6: Geometry of the phase grating mode

in its simplest form has been applied to anisotropic dielectric gratings like that of twisted liquid crystals [2,3]. This theory in the form applied to liquid crystals makes the assumption that the amplitude of the phase modulation of the emergent wavefront is smaller compared to grating period. This is equivalent to assuming that (i) the sample is thin, (ii) the birefringence is small and (iii) the periodicity of the medium is large compared to the wavelength of light. In effect here we assume that there is no appreciable diffraction taking place inside the medium, *i.e.*, the wave front is considerably corrugated only when it emerges out of the medium.

In the RN theory the emergent wavefront is described by

$$U(z) = A_0 \exp(j2\pi n_z t/\lambda)$$

where t is the thickness of the sample, A_0 is the amplitude of the incident plane wavefront and n_z is the refractive index for the vibration perpendicular to the twist axis at any point z given by

$$\frac{1}{n_z^2} = \frac{\sin^2\theta}{n_e^2} + \frac{\cos^2\theta}{n_0^2}$$

n_e and n_o being the principle refractive indices parallel and perpendicular to the director,respectively. The diffractiod pattern is then given by the Fourier transform of $U(z)$

$$\Sigma(K) = \int_{-\infty}^{\infty} U(z)\exp(-jKz)dz$$

Where

$$K = \frac{2\pi \sin\theta_d}{\lambda},$$

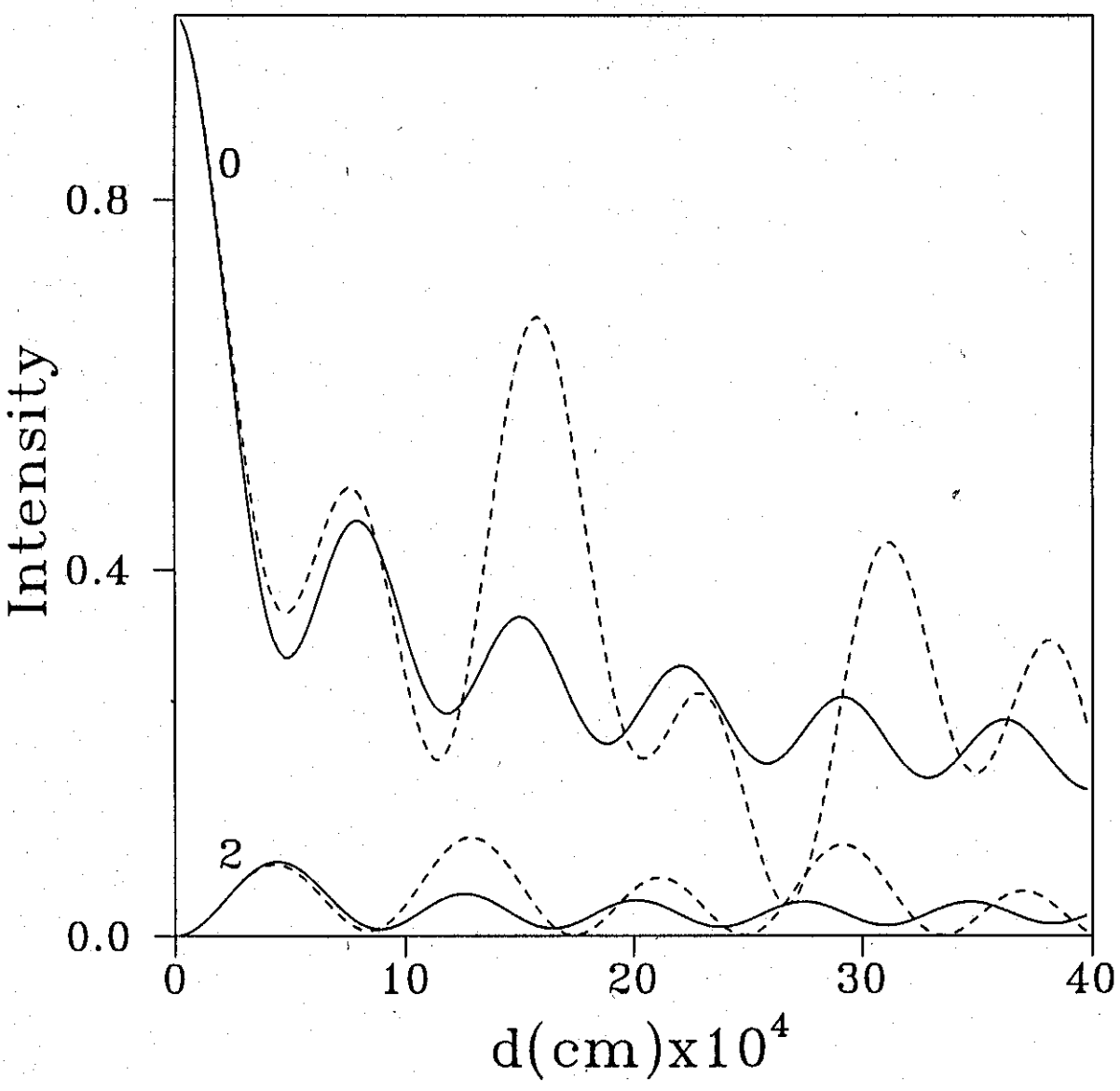

Fig 6.7: A comparison of the intensities in the central and second order of the phase grating diffraction pattern computed using RN theory (contineous) and RY theory (broken line) as a function of the sample thcikness 'd' for a π soliton lattice at $H = 22065$ with other parameters same as in Figure:6.2

θ_d being the angle of diffraction.

The above assumptions are not always valid in usual experimental situations. And in most of the situations the internal diffractions are important. In such cases a multiple beam analysis [11] wherein we consider more than one plane wave propagating inside the medium, is very useful, In this paper we follow the method of Rokushima and Yamakita [RY] [11]and compare the results with those obtained through Raman and Nath theory.

In the RY theory we Fourier expand the dielectric tensor and electromagnetic field components as

$$\epsilon_{ij}(z) = \sum_{l=-n}^{n} \epsilon_{ijl} \exp(jlqz)$$

$$E_i = \frac{1}{\sqrt{\epsilon_0}} \sum_{-n}^{n} e_{in}(x) \exp(-j(q_0 + nq)z)$$

$$H_i = \frac{1}{\sqrt{\epsilon_0}} \sum_{-n}^{n} h_{in}(x) \exp(-j(q_0 + nq)z)$$

where $q = \frac{2\pi}{P}$. and $q_0 = \sqrt{\epsilon_0} \sin\beta$

Mere β is the incidence angle with respect to a plane normal to the twist axis. Thus we can express the Maxwell's equations for the tangential field components in the zx plane in the form,

$$\frac{d\eta}{dx} = jC\eta \tag{6.6}$$

where, $\eta = \begin{bmatrix} e_y \\ h_z \\ e_z \\ h_y \end{bmatrix}$ *and* $C = \begin{bmatrix} 0 & -1 & 0 & 0 \\ \varepsilon_{yx}\varepsilon_{xx}^{-1}\varepsilon_{xy} - \varepsilon_{yy} + q^2 & 0 & 0 & -\varepsilon_{yx}\varepsilon_{xx}^{-1}\mathbf{q} \\ \mathbf{q}\varepsilon_{xx}^{-1}\varepsilon_{xy} & 0 & 0 & -\mathbf{q}\varepsilon_{xx}^{-1}\mathbf{q} + 1 \\ 0 & 0 & \varepsilon_{zz} & 0 \end{bmatrix}$

Hereε_{ij} are $(2n+1) \times (2n+1)$ submatrices with elements $\varepsilon_{ijnl} = \varepsilon_{ijl-n}$, $\mathrm{q} = \delta_{nl} q_l$, $q_l = lq + q_0$ and $e_{,}$, h_z, e_z, h, are (2n + 1) column matrices. Equation (6.6) is solved numerically for η.

In the simple theory of RN as the sample thickness increases the number of diffraction orders increases. While in the RY theory the number of diffraction orders increases up to a certain thickness beyond which it decreases. We compare in Fig 6.7 the results of RN and RY theories in the case of normal cholesteric soliton lattice. The intensities of the central and second orders are given as a function of the sample

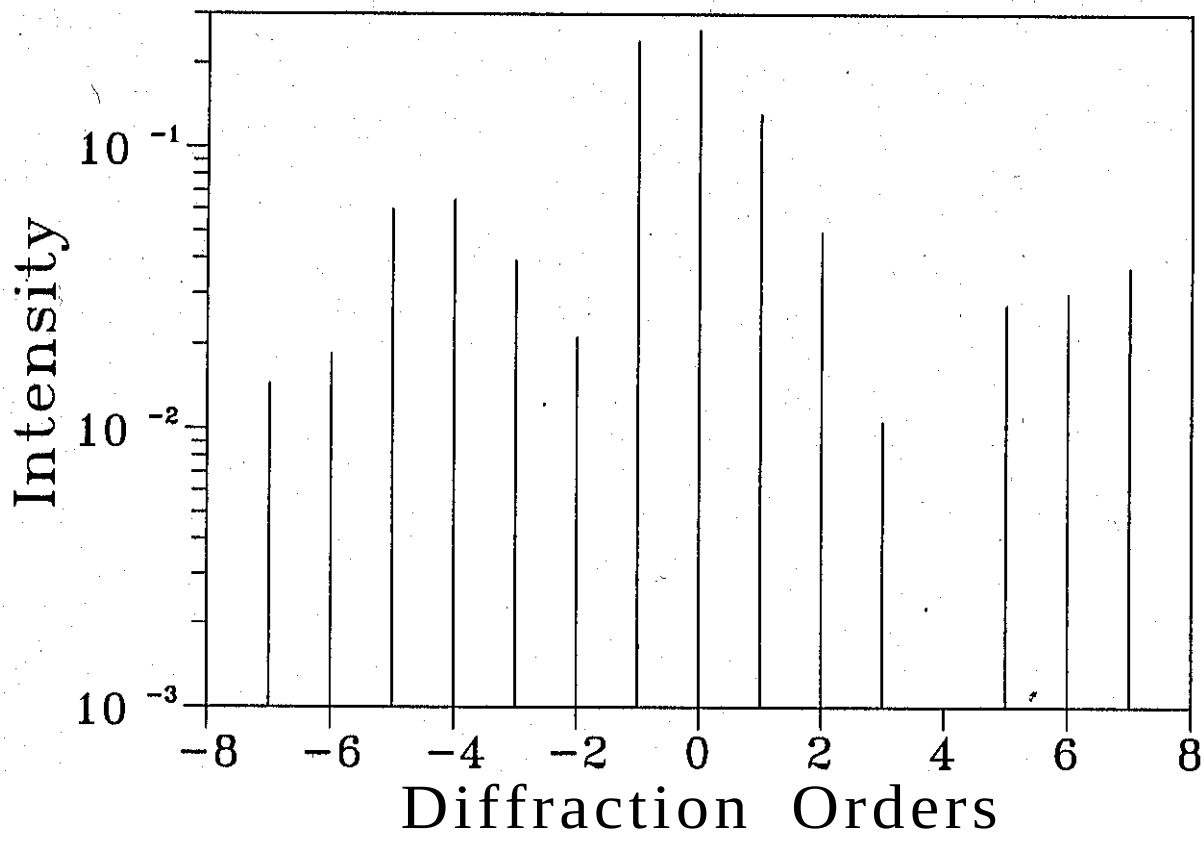

Fig 6.8: The asymmetry in the diffraction pattern of the π soliton lattice same as in figure:6.7 with $\omega = \pi/16$.

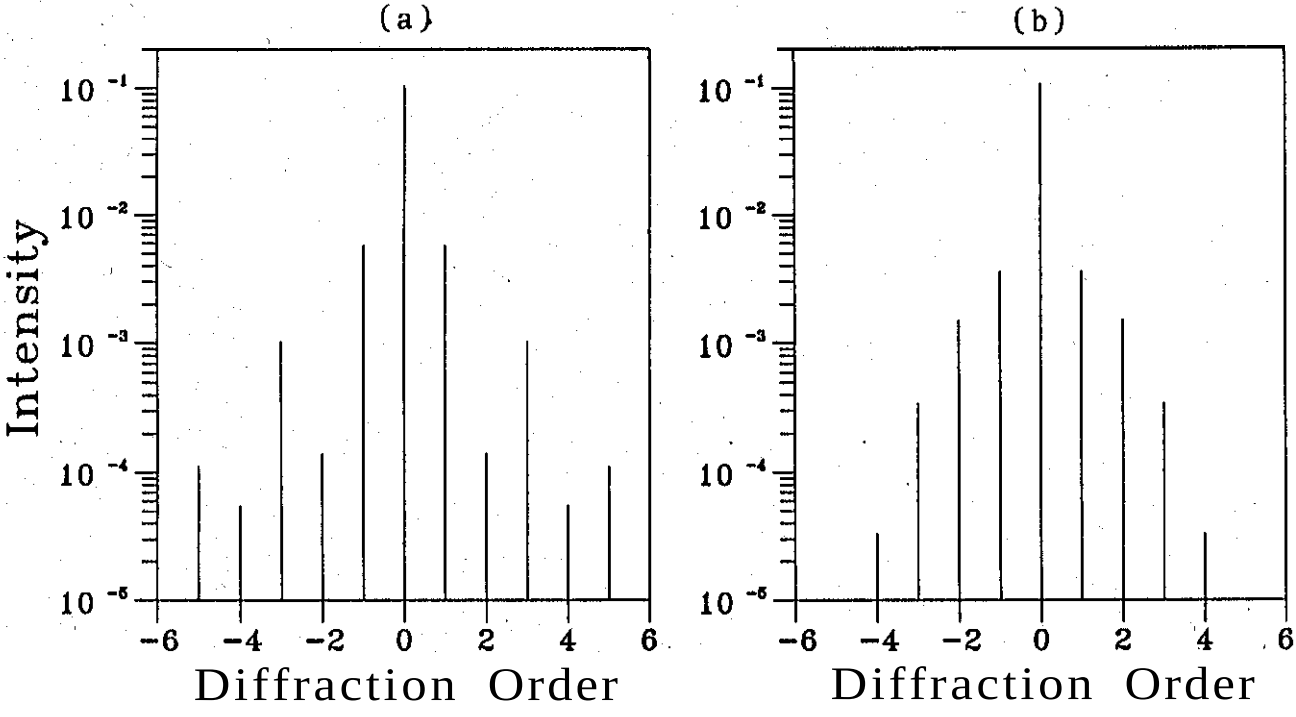

Fig 6.9: Diffraction due to the segregation of absorbing grains. For N-W soliton lattice (a) and for π soliton lattice (b). P $= 19\mu m$, and the grain refractive index $n = 1.505 + .02j$.

thickness. We see that the RN theory is valid only up to certain thickness (in our case 7μ). It must be remarked that in general in the RY theory (for cholesteric soliton lattice) each order is elliptically polarized. But at low values of the birefringence they are nearly linear states. In RN theory, however, they are strictly linear states.

When the angle of incidence w with respect to the field direction is such that $0 < w < \frac{\pi}{2}$ (see Fig.6.6) the diffraction pattern is asymmetric this is shown ifn Fig 6.8. This feature is typical of a soliton lattice. When the structure is absorbing we have also linear dichroism. Then the development of the soliton lattice can be easily recognized. Here we find for $w = 0$ all the orders to to be weak for positive dichroism. This implies that th'e weakly twisted regions are nearly parallel to the field.

We shall now consider the peculiar features associated with the ferrocholesteric soliton lattices. One important feature is the migration of the magnetic grains. The grains can either be transparent or absorbing. When the grains are absorbing the medium also become absorbing. Since the concentration of the grains along the twist axis is nonuniform this absorption will also be nonuriiforrn along the twist axis. This nonuniformity alone results in diffraction when the incident polarization is parallel to the twist axis. This kind of diffraction is peculiar to the soliton lattices in the sense that they are totally absent for undistorted system. This is depicted in Fig 6.9. In Fig 6.9a we show, the diffraction pattern due to N-W soliton lattice obtained for $\chi_a < 0$ materials. This is very different from diffraction of the soliton lattice in $\chi_a > 0$ materials (Fig 6.9b). The peculiar feature of the diffraction in N-W soliton lattice is that intensity fluctuates from order to order and we find the even orders to be less intense than the odd orders, whereas for the double π lattice the intensity decreases monotonically. This feature in the pattern could be used to distinguish N-W lattices of $\chi_a < 0$ materials from soliton lattices of $\chi_a > 0$ materials.

In these calculations we have ignored the Faraday rotation due to the magnetic grains. This parameter itself can considerably alter the diffraction pattern even in simple ferrocholesterics [12]

6.3.1 Test for twist induced biaxiality

It is now well established that cholesteric liquid crystals are in principle biaxial [13] The inherent chirality arid the hindered rotation of the molecule due to the twist

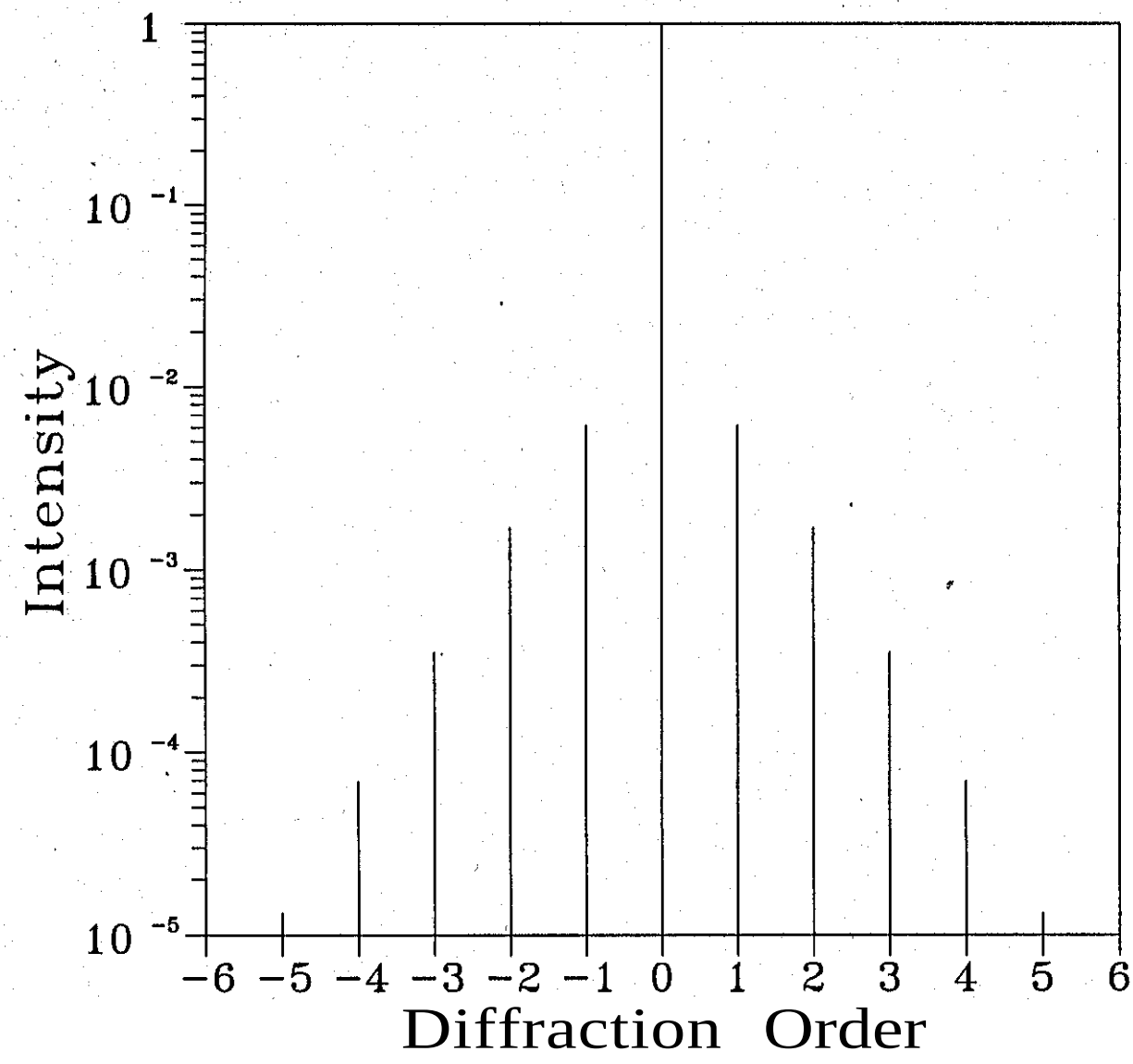

Fig 6.10: The computed diffraction pattern due to the variation of twist induced biaxiality along the twist axis of a π soliton lattice.

are the two mechanisms proposed [13] to expain this biaxiality. It has been argued that the induced bixiality increases with increase in twist. To our knowledge, no direct optical measurements have been purposed to verify this. It is easy to see that twist induced bixiality in the soliton lattice will vary as function of z resulting in a fluctuation in refractive index $n_{\|}$. As a result of this effect, for the incident light with polarization parallel to the twist axis, we get a diffraction pattern. In Fig 6.10, we show one such diffraction pattern computed by assuming th'e bixiality to vary linearly with twist. The pattern appears even for $\Delta n_{\|}$ as small as 5×10^{-3}. Thus, the method appears to be sensitive enough to reveal the. twist induced bixiality.

References

[1] Shtrikman,S. and Tur,M., 1974, J. *Opt. Soc. Am.,* 64, 1178

[2] Chandrasekher,S. and Prasad,J.S., 1969, *Physics of solid state,* Edited *by* Balakrishna

[3] Suresh,K.A., Sunil Kumar,P.B. and Ranganath,G.S., 1992, *Liquid Crystals,* **11,** 73

[4] Oldano,C., 1989 *Phy. Rev.,* A15, 6014

[5] Sunil Kumar,P.B. and Ranganath,G.S., *Mol. Cryst. Liq. Cryst.,* 196, (1991) 27

[6] Berreman,D.W., 1972, J. *Opt. Soc. Am.,* 62, 502

[7] Arnold,V.I., 1978 *Clasical Mechanics, Springer-Verlag*

[8] Belyakove,V.A. and Dmitrienkov,V.E., 1989 *Optics of Chiral Liquid Crystals, Soviet Scientific Reviews,* A 13

[9] Yuvraj Sah and Suresh,K.A., *Private Communication*

[10] Raman,C.V. and Nagendra Nath,N.S, 1935, *Proc. Indian. Acad. Sci,* A2, 406

[11] Rokushima,K. and Yamakita,J., 1983, J. *Opt. Soc. Am.,* 73, 901

[12] Yuvraj Sah, Suresh,K.A. and Ranganath,G.S., 1993, *Liquid Cryatals* (in press)

[13] Yaniv,Z., Chidichimo,G., and Doane,J.W., 1983, *Phy.Rev.* A 28, 3012

APPENDIX A
GEOMETRICAL THEORY OF DIFFRACTION

Geometrical theory of diffraction(GTD) deals with Fresnel diffraction. It is a recapitulation of Young's idea of diffraction, viz., diffraction is a manifestation of interference between the light waves directly transmitted by an aperture and waves emitted by the boundary. From the point of mathematical computations this theory is quite simple and straightforward. Also it is possible to easily and physically account for many of the strange and peculiar facts associatkd with Fresnel diffraction patterns. GTD has a long history. Many of its essential steps were worked out by the Raman school [1]. Later thery were rediscovered by the successive investigators in particular by Keller [2]. For an historical account see ref [3].

Diffraction by thin edge of arbitrary shape

'Using Krichhoff's theory one can in principle calculate the Fresnel diffraction pattern of the obstacles and apertures. But the calculations are difficult and wherever one got the answers a physical understanding was elusive. In 1888 Maggi showed that the Kirchhoff diffraction integral may be reduced to a sum of (i) a wave propagating according o the laws of geometrical optics called the geometrical wave, and (ii) a wave originating from every point on the boundary of the obstacle or aperture - called the boundary wave. For an incident spherical wave consider a cone forrned by the rays emitted by the source and the boundary of the aperture. Then this boundary wave can then be written as:

$$v_b = \frac{1}{4\pi}\int_s \left[\frac{e^{ik\rho}}{\rho}\frac{e^{ikr}}{r}\frac{\cos\theta_1}{1+\cos\theta_3}\sin\theta_2\right] ds$$

where,

ρ = distance of the point of integration from the source,
r = distance of the point of integration from the point of obeservation,
θ_1 = angle of reflection at the cone surface,
θ_2 = angle of incidence at the curved element of the edge,
θ_3 = angle of reflection at the edge.

The above integral is highly oscillatory. Thus substantial amount of contribution comes from only a few points [1,5,1] called poles, These are points on the boundary

where the phase is stationary with respect to the movement on the boundary curve s. This condition of stationarity of phase on the contour s gives the reflection condition

$$\cos\theta_2 = -\cos\theta_3$$

Thus at any point of observation the boundary wave contribution is essentialy reduced to that from a few points on the boundary. Ramachandran [6] showed that these contributions will have an additional phase of $\pm\pi/4$ depending upon whether the point is one of maximum or minimum path with respect to the point of observation.

Corner radiation

This method of stationary phase fails at the sharp corners of obstacles and appertures. Kathavate pointed out that these points acts as sorces of spherical radiation [7]. We find the corner radiation to be given by [8]:

$$v_c = \frac{i\lambda \sin\xi}{4\pi} \frac{\cos(n,\mathrm{r})}{r} \exp(-ikr) \frac{z^2}{d_1 d_2} \qquad (A.2)$$

where,

ξ = angle between the two local tangents to the boundary at the corner

= the perpendicular distance from the point of observation to the sorce

d_1, d_2 = components of the vector joining the foot of the perpendicular to the corner

Surface diffraction

So far we have restricted ourselves to infinitly thin diffracting objects. In the case of objects wit11 finite lateral thickness the diffraction pattern can be very different as was shown by Raman and Krishan [9]. In the case of smooth objects light actualy creeps along the surface, always leaving the surface along the local tangent. This explains the observed difference between the Poisson spot intensity of a disc and a sphere of equal diameter [9].

Generalized *Fermat's* principle

All the avove effects could be accounted as the result of one principle known as the generalized fermats principle [10]. This states that light is always so diffracted that

the path chosen from the source to the boundary and to the point of observation is an extrimum.

By appealing to Sommerfeld's theory of diffraction at a straight edge [11] Keller worked out the amplitude of the diffracted field. When the light is incident at an angle α on a straight edge thid field is given by:

$$U = U_i D_0 \frac{e^{ikr}}{\sqrt{r}} \tag{A.3}$$

with

$$D_0 = -\frac{\exp(-i\pi/4)}{2(2\pi k)^{1/2}\sin\alpha}\left\{\frac{1}{\cos[(\phi-\phi_0)/2]} \pm \frac{1}{\cos[(\phi+\phi_0)/2]}\right\}$$

U_i is the incident wave, ϕ and ϕ_0 are the angle made by the incident and diffracted wavefronts with the diffracting plane. We take the $+$ (or $-$) sign when the incident clctric polarization is parallel (or perpendicular) to the screen.

This gives the diffracted rays travelling on a cone symmetric about the edge. For normal incidence this predicts the edge to emmit cylindrical waves as first suggested by Raman [1] and Rubunowicz [5].

Keller argued that the edge with a finite curvature emits cylindrical waves locally. Thus the diffracted wavefront in this case will be curved. From light flux conservation Keller showed that, the diffracted rays in such cases to be given by:

$$U = D_o U_i \frac{e^{ikr}}{[r(1+r/\rho_1)]^{1/2}} \tag{A.4}$$

Where ρ_1 denotes the distance from the edge to the caustic measurctl negatively in the direction of propagation. Hence as we cross the caustic U gets an extra phase of $\pi/2$, and the expression itself is not valid at and near the caustic.

Applications of ***GTD***

GTD can be used to simulate the tliffraction pattern of complicated objects. These patterns are found to agree very well with the experimental results [12]. However, it has its own limitations. For example it does not smoothly go over to the Fraunhaufer pattern and gives singularities at the caustics. Many of this problems are overcome in the Uniform theory of diffraction which has been dealt with exhaustively by McNamara *et. al.,* [13]. We will now look at some of the important results

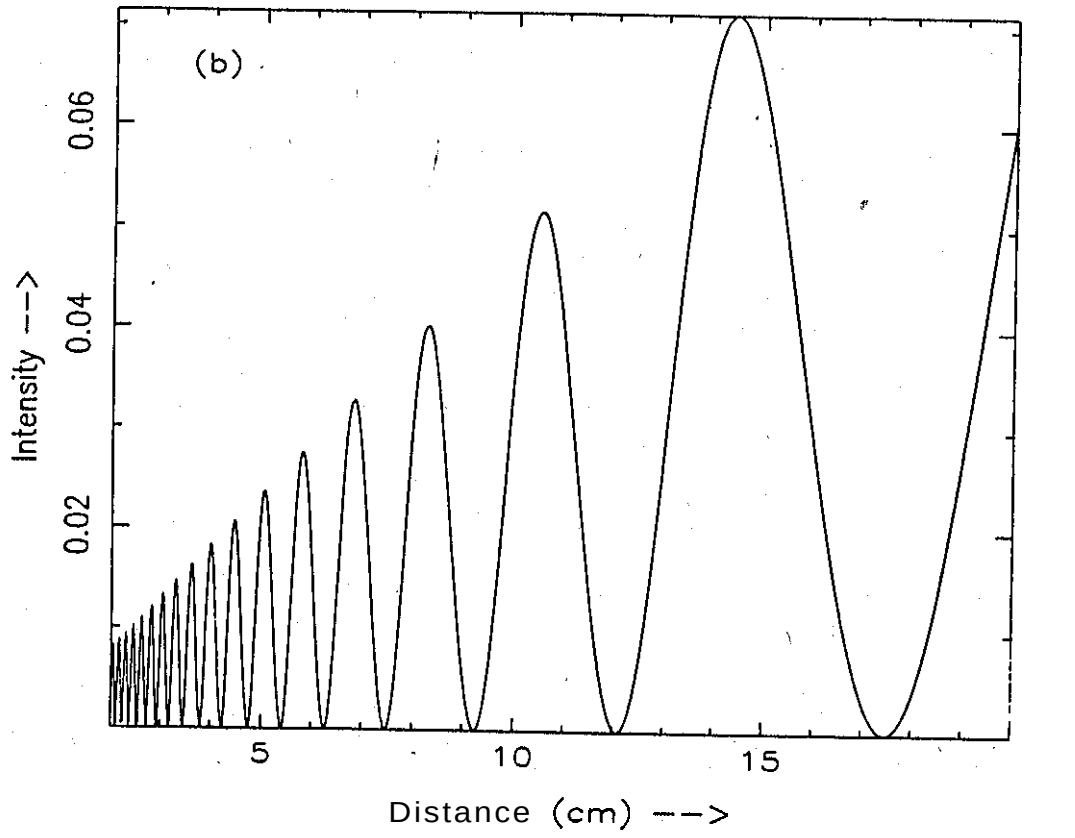

Fig A.1: Dependence of poisson spot intensity with distance from the diffracting screen for an elliptic disc of major diameter 1.0 cm and minor diameter 0.99 cm.

(a)

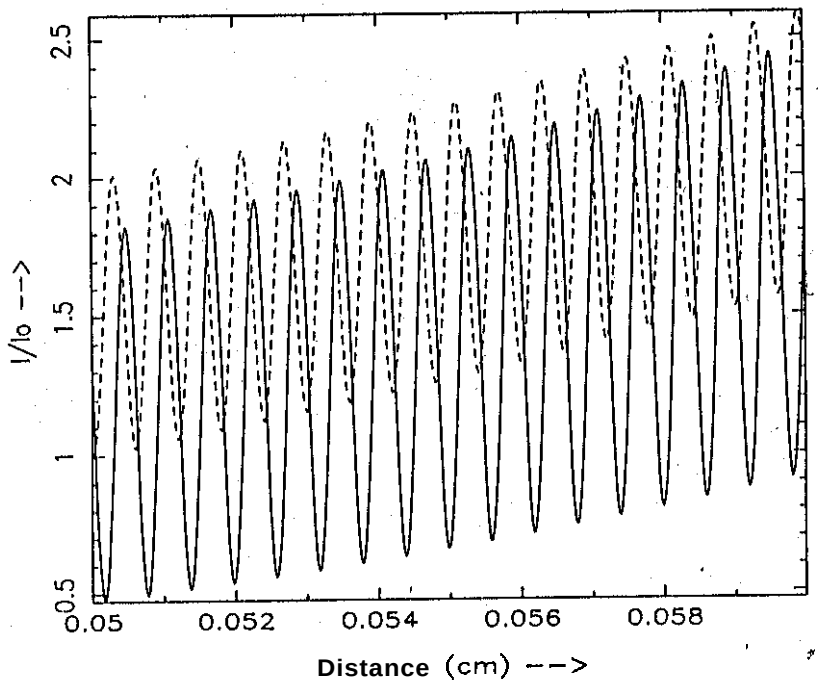

(b)

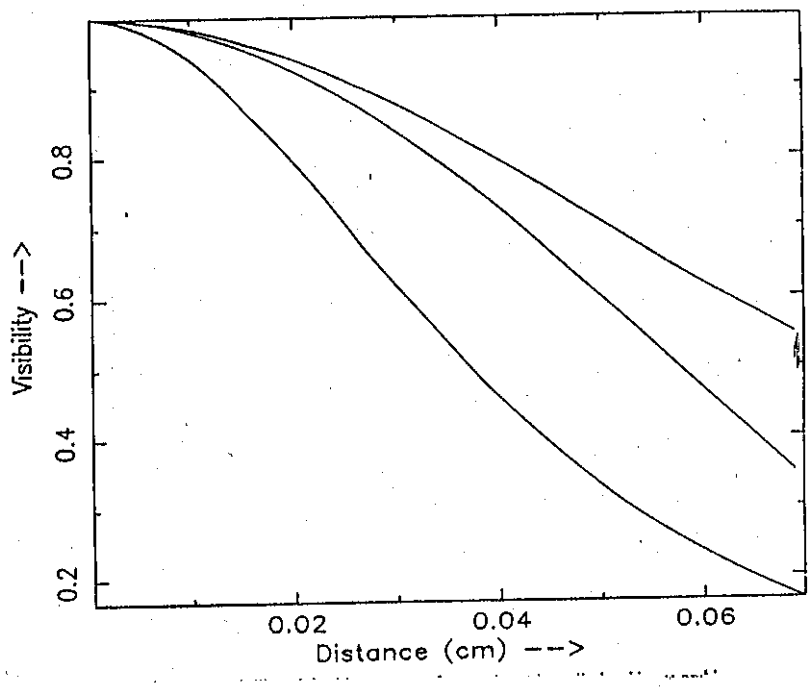

Fig 2 **(a)** Fringe system for a cylinder (broken line) of radius 0.1 cm and strip (continuous line) of the same width at a distance 2 cni. Abscissa shows the distance from the center of the pattern as we move across the shadow. Ordinate depicts the intensity scaled with respect to the intensity at the center. (b) Visibility of the fringe system. Upper and lower curves are the visibility of the fringe system of a cylinder at a distance of **4** cm and **2** cm respectively. The middle curve shows the fringe visibility of the strip at these two distances. In this case the visibility is independent of the distance from the strip.

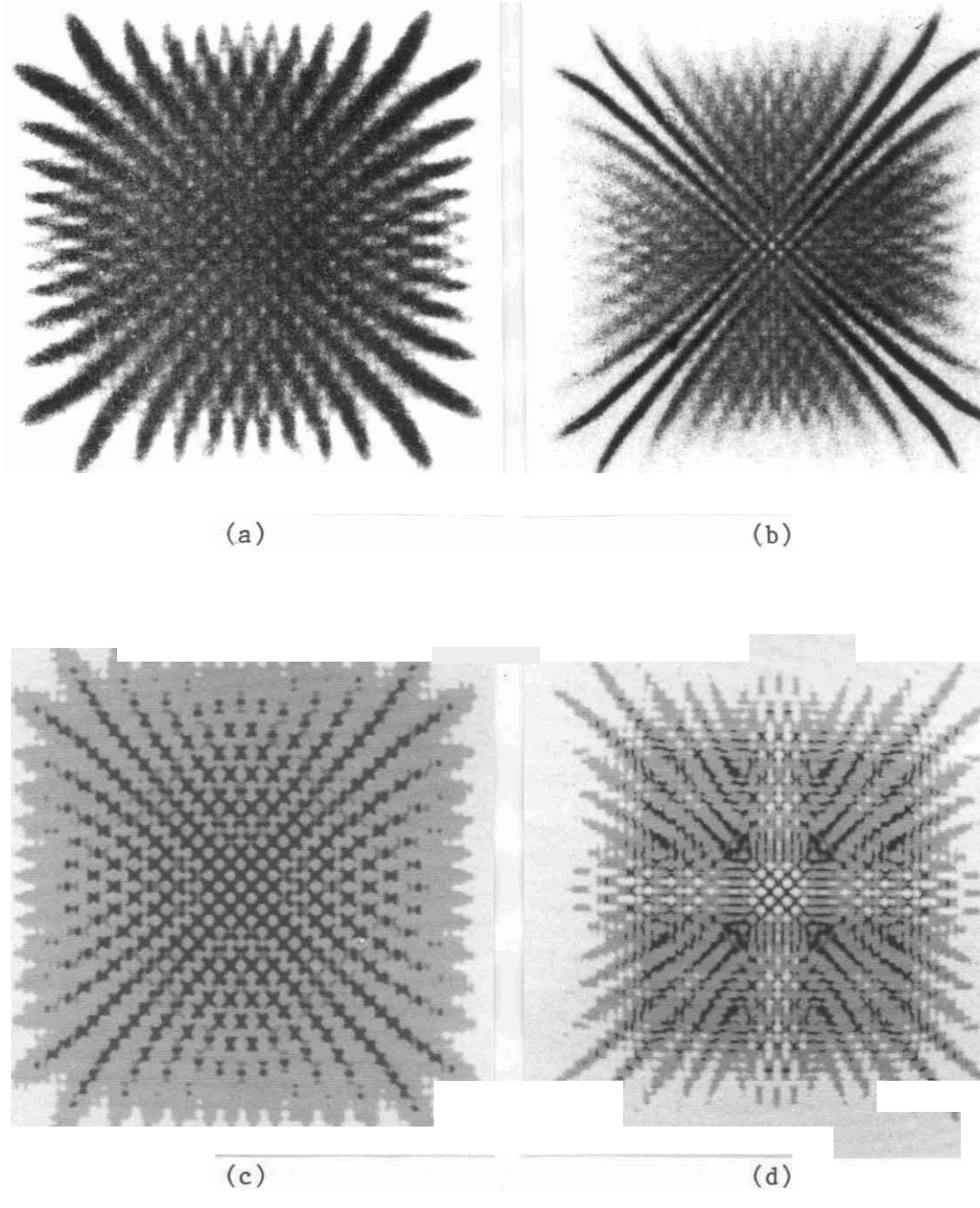

Fig **A.3:** The diffraction pattern in the shadow of a square obstacle. (a) and (b) are the pattern obtained from experiments (after reference [7]) for the monochromatic and polychromatic light respectively. ***(c)***and (d) depicts the same pattern simulated using GTD.

obtained by using GTD.

Poisson spot:- We have already mentioned the existence of a bright central spot in the case of circular disks. This is due to the constructive intefernce of boundary waves from all the points on the boundary. However an interesting possibility exists in the case of a rectangular and elliptic disks. If we ignore the contribution due to the corner radiations which are generally very weak then in both cases we have four poles contributing to the central spot. The contribution from opposite poles are in phase at the center. But the two pair pole radiations will. be in and out of phase as we recede from the plane of the object resulting in central spot intensity fluctuation. In Fig A.1. we show this intesity fluctuation in the case of an elliptic disk.

Surface versus edge diffraction:- We have allready mentioned that in the case of smooth objects with finite lateral thickness light creeps along the surface. To illustrate this phenomena we will take a strip and a cylinder of equal width as an example. The creeping effect in cylinder makes the diffraction pattern to be very different from that of a strip in terms of fringe position and visibility. This is illustrated in Fig A.2.

Polychromatic light diffraction:- To get the diffraction pattern due to white light all we have to do in GTD is to add the contribution due to the individual component of incident light. The computed pattern for a square disk agrees very well with the experiments. In Fig **A.3** we compare the experimetal diffraction pattern in the shadow region of a square obstacle obtained by Kathavate [7] with the same simulated using GTD.

Effect of polarization:- We see that the value of D_0 is different for the two orthogonal polarizations. This leads to an interesting answer in the case of diffraction by a square disk. Here when the incident polarization is parallel to one pair ofeclges it is orthogonal to the other pair of edges. Thus the diffraction pattern in this case will have only a two fold symmetry. We get the strict four fold symmetry only when the incident light is unpolarized or is linearly polarized at an angle $\pi/4$ with respect to the edge.

Appendix **A**

References

[1] Raman,C.V., 1941, *Sayaji Rao Gaekwar foundation lectures on physical optics* (Indian Academy of Sciences)

[2] Keller,J.B., 1956, IRE *Trans. Antennas and Propagation,* **AP24**, 312

[3] Sunil Kumar,P.B. and Ranganath,G.S., 1991, *Curr. Sci., 20,* 26

[4] Rubinowicz,A., 1917, *Ann. Phys, 53,* 257

[5] Rubinowicz,A., 1924, *Ann.. Phys,* **73,** 339

[6] Ramachandran,G.N., 1945, *Proc. Indian Acad. Sci.,* **A21**, 165

[7] Kathavate,Y.V., 1945, *Proc. Indian Aca. Sci, A21,* 177

[8] Miyamoto,K. and Wolf,E., 1962, J. *Opt. Soc. Am., 52,* 615,626

[9] Raman,C.V. and Krishnan,K.S., 1926, *Proc. Phys. Soc. (London), 38, 350*

[10] Keller,J.B., 1962, J. *Opt. Soc. Am, 52,* 116

[11] Sommerfeld, A., 1896, *Math. Ann., 47,* 317

[12] Sunil Kumar,P.B. and Ranganath,G.S., 1991, *Pramana* J. *Phys., 37,* 457

[13] Mcmamare,D.A.,Pistorius,C.W.I. and Malherbe,J.A.G., 1990, *Introduction to the uniform geometrical thiory of diffraction* (Artech House, Norwood)

CHAPTER V

TOPOLOGICAL SOLITON$ IN FERRONEMATICS AND FERROCHOLESTERICS

5.1 Introduction

We have already seen that a magnetic field alters considerably the structure of the defects in liquid crystals. We also saw that the fields required for the elastic deformation of ferronematics is much less compared to that of normal nematics. In the limit of a good mechanical coupling between the host nematic and the grains 'in magnetic fields we get new types of topological defects in these systems. The diamagnetic anisotropy of the host and the magnetization of the grains strongly influence the structure of these defects, in the presence of a magnetic field [1].

In 1970 Brochard and de Gennes [4] studied on theoretical grounds, ferrocholesteric liquid crystals (FCh) – wherein the ferromagnetic grains are aligned with their magnetization m along the local director.It is well known that when a magnetic field H is applied perpendicular to the twist axis of normal cholesterics they undergo a transition to the nematic state at a critical field H_{Ch-N} [2,3]. It was also pointed out by earlier workers that for fields $0 < H < H_{Ch-N}$ the twist angle θ varies non-linearly with distance along the twist axis [2,3] leading to a lattice of 180^0 (or π) twist walls. In recent literature this has been described as a soliton lattice. This transition is purely due to the local diamagnetic anisotropy χ_a of the cholesterics. Brochard and de Gennes [4] worked out the magnetic field effects in ferrocholesteric by ignoring 'the intrinsic diamagnetic anisotropy of the host matrix. They predicted a soliton lattice of 360^0 (or 2π) twist walls to develop in these systems. Since it is now known [5] that the diamagnetic anisotropy of the host does influence the behaviour of these ferro systems in a magnetic field, it will also be interesting lo work out the unwinding of ferrocholesterics in a magnetic field.

In this chapter we will discuss the field inducetl soliton states in ferronematics

and ferrocholesterics

5.2 Ferronematics

While discussing the Freederickzs transition in ferronematics we ignored grain segregation. This was reasonable since the associated distortions were small. But in topological defects distortions are rather large. Hence we also consider grain segregation under field induced distortions. We confine ourselves to the case where the grain magnetization m is along the nematic director n.

5.2.1 Positive diamagnetic anisotropy

Consider an infinite sample of a ferronematic in the presence of a magnetic field. A *2n* wall (planar soliton) connecting two regions with grain magnetization m aligned along the magnetic field is a permitted solution. Far away from a given plane $z = 0$ on both sides, the director will be aligned along the field, with magnetization m parallel to H. And most of the 2π distortion is confined to a narrow region of space. Such narrow twist walls have also been tkrmed as 'planar solitons' [6] We will now work out the structure of this defect. The free energy density in the one constant approximation for a dilute solution of grains is:

$$F_d = \frac{k}{2}\left(\frac{\partial \theta}{\partial z}\right)^2 - \frac{\chi_a H^2}{2}\sin^2\theta - fmH\sin\theta + \frac{fk_BT}{V}In(f) \qquad (5.1)$$

where,

H	=	magnetic field along the x−axis
k	=	elastic constant
χ_a	=	diamagnetic anisotropy
m	=	magnetization of the individual grains
V	=	volume of the individual grains
f	=	volume fraction of the grains
θ	=	angle w.r.t. y−axis
k_B	=	Boltzmann constant
T	=	temperature

Minimizing the net energy with respect to f and θ, we get

$$-\rho_0 H\sin\theta + \ln f + 1 = 0 \qquad (5.2)$$

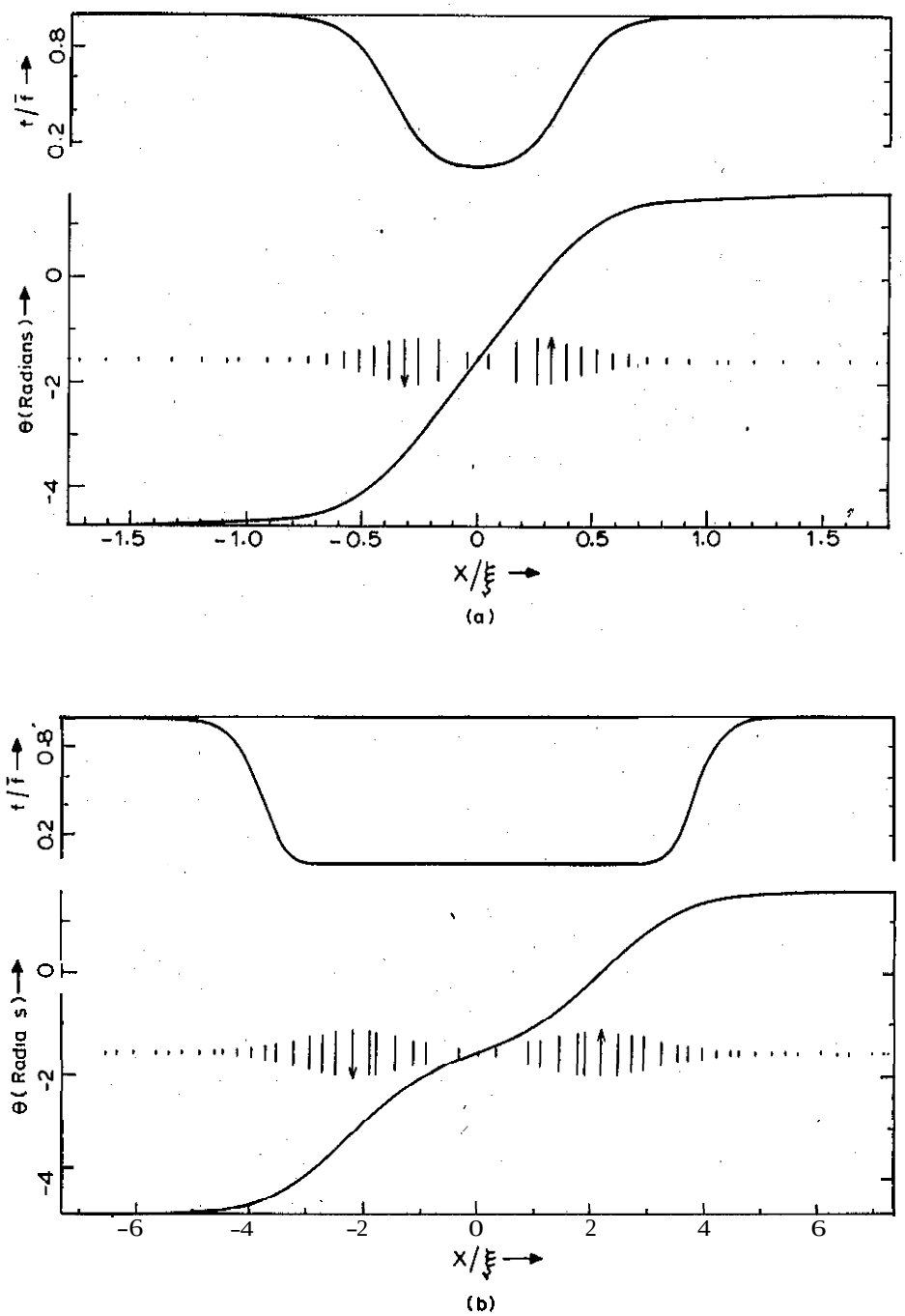

Fig 5.1: Director profile, tilt and concentration $f/\tilde{f}$ for 2π twist planar soliton for $k = 0.5 \times 10^{-6}$ dynes, $|\chi_a| = 10^{-6}$ cgs units, $\rho_0 = 0.02$ Gauss-', $\tilde{f} = 10^{-3}$, and $H_c = 78$ Gauss, for (a)$H = 70$, (b)$H = 1000$ Gauss.

and

$$\frac{\partial^2\theta}{\partial z^2} = \frac{\sin(2\theta)}{2\xi_1^2} - \frac{\psi\cos\theta}{\xi_2^2} \tag{5.3}$$

where,

$$\rho_0 = (mV/k_BT) \qquad \psi = f/\bar{f}$$

$$\xi_1^2 = k/(\chi_a H^2) \qquad \xi_2^2 = k/(m\bar{f}H)$$

here $\bar{f}$ is the average volume fraction of the grains in the undistorted state. The net magnetization due to the grains is $M = \bar{f}m$

The parameter ρ_0 can be considered as a measure of the degree of segregation of the grains. At $z = \infty$ the volume fraction of the grain f approaches its mean value $\bar{f}$ and $\theta =$ will be an odd multiple of $\pi/2$. Solving Equation **(5.2)** with this boundary conditions we get

$$\psi = \exp[\rho_0(\sin 0 - 1)H] \tag{5.4}$$

Here it is assumed that when the grains are expelled out of the central region to the outer regions, the average grain concentration remains unaltered at $z = \pm\infty$.

Equations **(5.3)** and **(5.4)** are solved numerically with the boundary conditions:

$$\frac{\partial\theta}{\partial z} = 0 \text{ at } z = \pm\infty, \quad \theta = \frac{\pi}{2} \text{ at } z = +\infty \text{ and } \theta = \frac{-3\pi}{2} \text{ at } z = -\infty.$$

At low fields the magnetic energy due to the diamagnetic anisotropy is negligible. Thus at these low fields **(5.3)** allows the familiar Brochard-de Gennes 2π planar soliton solution. As field increases the diamagnetic energy becomes important. From **(5.1)** and **(5.4)** we see that above a critical value of the magnetic field given by:

$$H_c = \frac{m\bar{f}}{\chi_a}\exp(-2\rho_0 H_c)$$

the diamagnetic term in the free energy is higher than the magnetic energy due to the grain magnetization. Thus for $H > H_c$ the 2π planar soliton should become unstable. In Fig **5.1** we compare the structure and grain profile of the planar soliton for H above and below the critical field H_c. It is clearly seen that above H_c the 2π

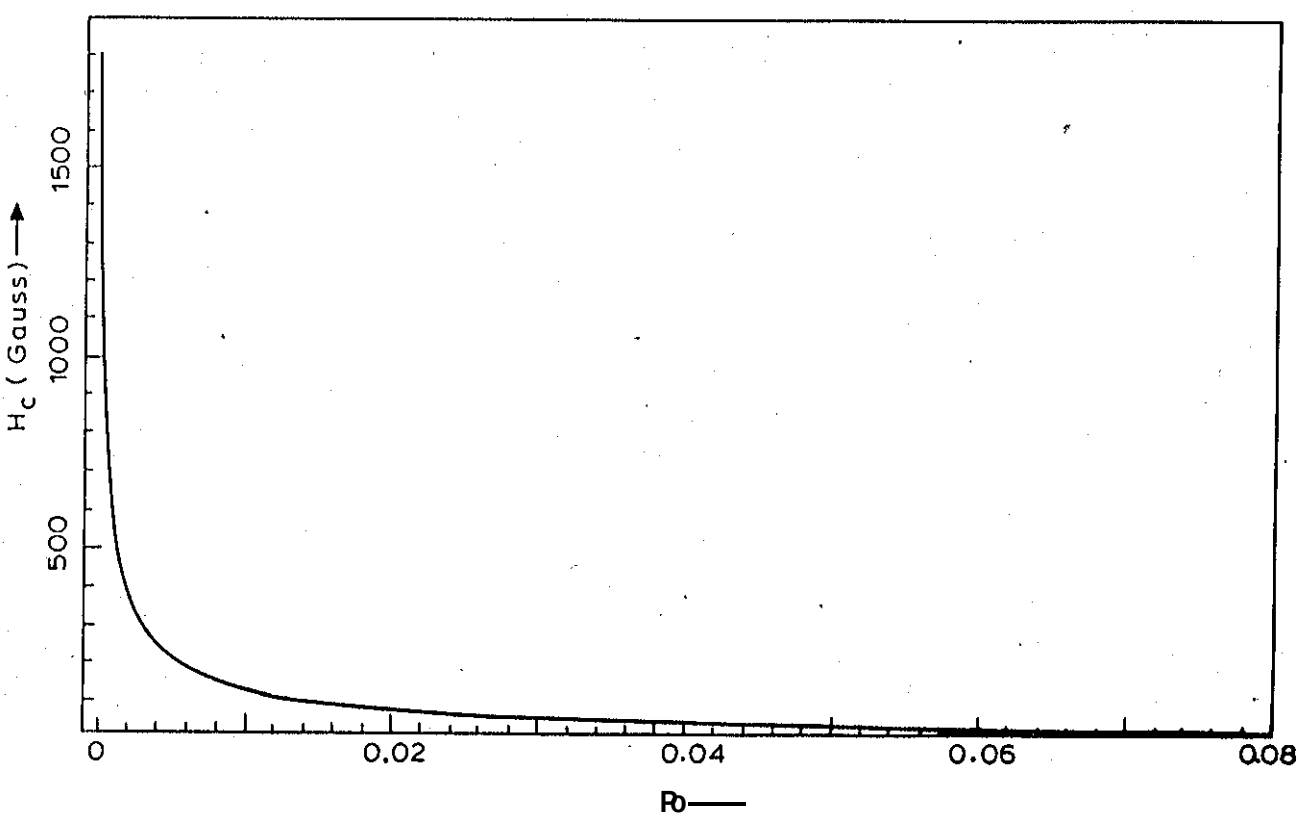

Fig 5.2: Variation of the critical field H_c pith the segregation parameter p ~ .

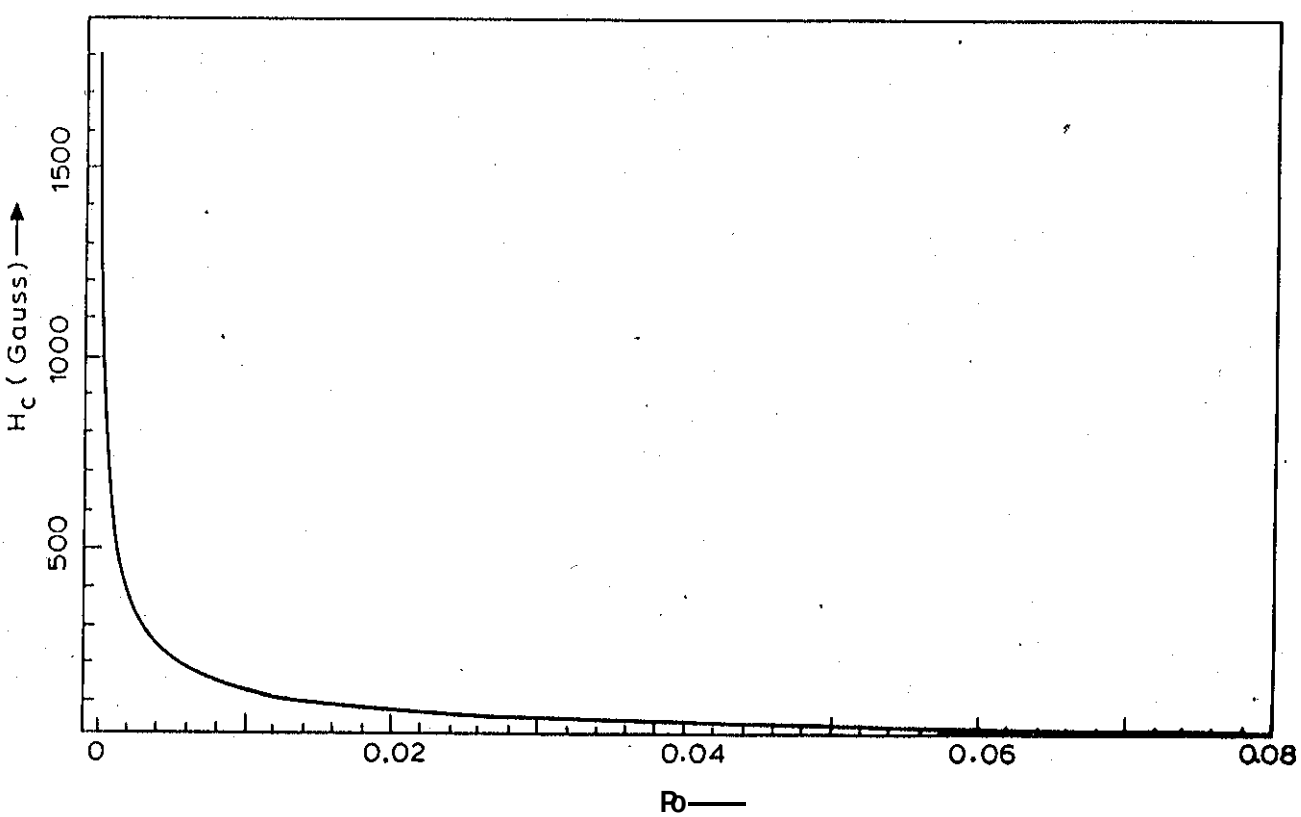

Fig 5.2: Variation of the critical field H_c pith the segregation parameter p ~ .

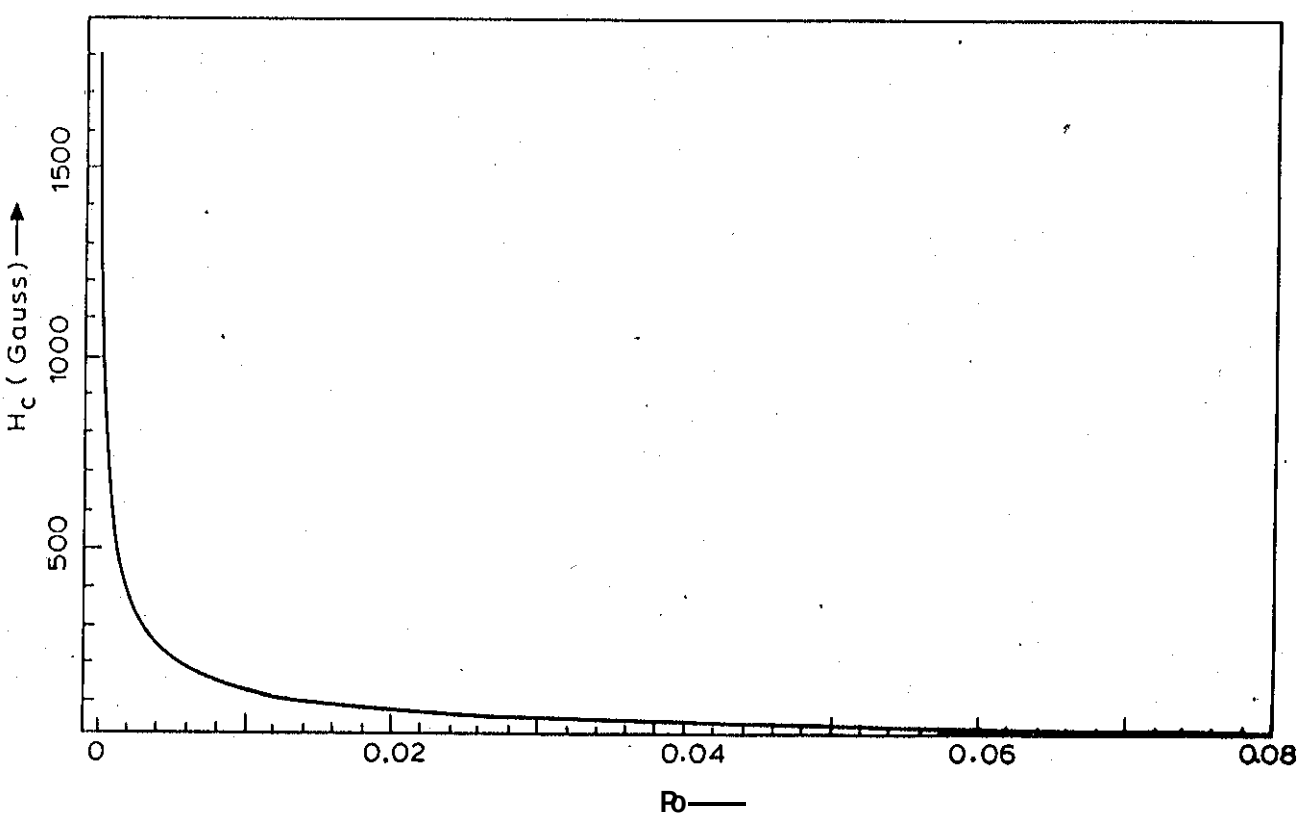

Fig 5.2: Variation of the critical field H_c pith the segregation parameter p ~ .

wall splits into two r walls. As is to be expected the magnetic grains move out of the central region. This segregation increases with increasing field. The critical field H_c decreases rapidly with ρ_0. This is shown in Fig 5.2. Another interesting feature is that though the splitting takes place for fields above H_c the distance of separation between the two π walls is more sensitive to ρ_0, increasing ρ_0 increases the distance of separation between the π walls.

The symmetry of the system also permits us to construct a linear soliton of the Mineev-Volovik type [6,7] which has cylindrical symmetry. Here as we move radially away from the center the the director rotates through π from a state where m is antiparallel to H to m parallel to H. But its structure and energetics cannot be worked out without the higher gradient terms in the free energy. This is akin to a similar problem in normal nematics with M = 0 [6,8]

5.2.2 Negative diamagnetic anisotropy

Here the tendency of the diamagnetic anisotropy of the molecules is to make n to align in a plane perpendicular to the magnetic field while the magnetization m tries to be parallel to the field. Thus we consider director distortions of the form n = (n,, n_α, n_z) in cylindrical polar coordinates where:

$$n_r = \sin\theta\ \cos(\varphi - a),\ n_\alpha = \sin\theta\ \sin(\varphi - a),\ n_z = \cos\theta$$

θ being the angle w.r.t. H and φ is the azimuthal angle. The free energy density is now given by:

$$\begin{aligned} F_d = \quad & \frac{1}{2}\left[\left(k_{11}\cos^2\theta + k_{33}\sin^2\theta\right)\cos^2(\varphi - a) + k_{22}\sin^2(\varphi - \alpha)\right]\left(\frac{\partial\theta}{\partial r}\right)^2 \\ & + \frac{1}{2r^2}\left(\frac{\partial\varphi}{\partial\alpha}\right)^2\left[\left(k_{33}\sin^2\theta + k_{22}\cos^2\theta\right)\sin^2(\varphi - \alpha)\right. \\ & \left. + k_{11}\cos^2(\varphi - a)\right]\sin^2\theta + \frac{\chi_a H^2}{2}\cos^2\theta + \frac{mH}{2}\cos\theta \end{aligned} \tag{5.5}$$

This leads to the following Euler equation :

$$\left[\left(k_{33}\sin^2\theta + k_{22}\cos^2 8)\,\sin^2(\varphi - a) + k_{11}\cos^2(\varphi - a)\right]\sin^2\theta\frac{\partial^2\varphi}{\partial r^2} = \right.$$
$$\frac{\sin[2(\varphi - a)]}{2}\left\{\left[\left(-k_{11}\cos^2\theta + k_{33}\sin^2\theta\right) + k_{22}\right]\left(\frac{\partial\theta}{\partial r}\right)^2\right. \qquad (5.6)$$
$$+\left[k_{33}\sin^2\theta + k_{22}\cos^2\theta - k_{11}\right]\frac{\sin^2\theta}{r^2}\left(2 - \frac{\partial\varphi}{\partial\alpha}\right)\frac{\partial\varphi}{\partial\alpha}$$
$$\left.+\left[k_{22} - k11\right]\sin(2\theta)\frac{1}{r}\frac{\partial\theta}{\partial r}\frac{\partial\varphi}{\partial\alpha}\right\}$$

The above equation permits the solutions $\varphi = a$ and $\varphi = a + \pi/2$.

When $\varphi = a$ *i.e.*, for the all radial structure θ is given by:

$$2[1 + \epsilon'\cos(2\theta)]\frac{\partial^2\theta}{\partial r^2} = \frac{(1 + \epsilon')\sin(2\theta)}{r^2} - \frac{2(1 + \epsilon')\cos(2\theta)}{r}\frac{\partial\theta}{\partial r} \qquad (5.7)$$
$$+\frac{\sin(2\theta)}{\xi_1^2} + \frac{2\sin\theta}{\xi_2^2} + 2\epsilon'\sin(2\theta)\left(\frac{\partial\theta}{\partial r}\right)^2$$

Where

$$\xi_1^2 = \frac{k'}{\chi_a H^2} \qquad \xi_2^2 = \frac{k'}{mfH}$$

$$\epsilon' = \frac{k_{11} - k_{33}}{k_{11} + k_{33}} \qquad k' = \frac{k_{11} + k_{33}}{2}$$

For $\varphi = a + \pi/2$ the structure is all circular and θ is given by the equation

$$2(1 + \varepsilon'')\frac{\partial^\theta}{\partial r^2} = \frac{\sin(2\theta)}{r^2}(1 - \varepsilon'' + 2\varepsilon''\cos(2\theta))$$
$$-\frac{sin(2\theta)}{\xi_1^2}\ \mathbf{t}\ \frac{2\sin\theta}{\xi_2^2} - \frac{2(1 + \varepsilon'')}{r}\frac{\partial\theta}{\partial r} \qquad (5.8)$$

Where

$$\xi_1^2 = \frac{k''}{\chi_a H^2} \qquad \xi_2^2 = \frac{k''}{mfH}$$

$$\epsilon'' = \frac{k_{22} - k_{33}}{k_{22} + k_{33}} \qquad k'' = \frac{k_{22} + k_{33}}{2}$$

It is clear from (5.7) and (5.8) that the orientation at $r \to \infty$ is given by the magnetic torque alone. This permits the director orientation at $r = \infty$ to be given by

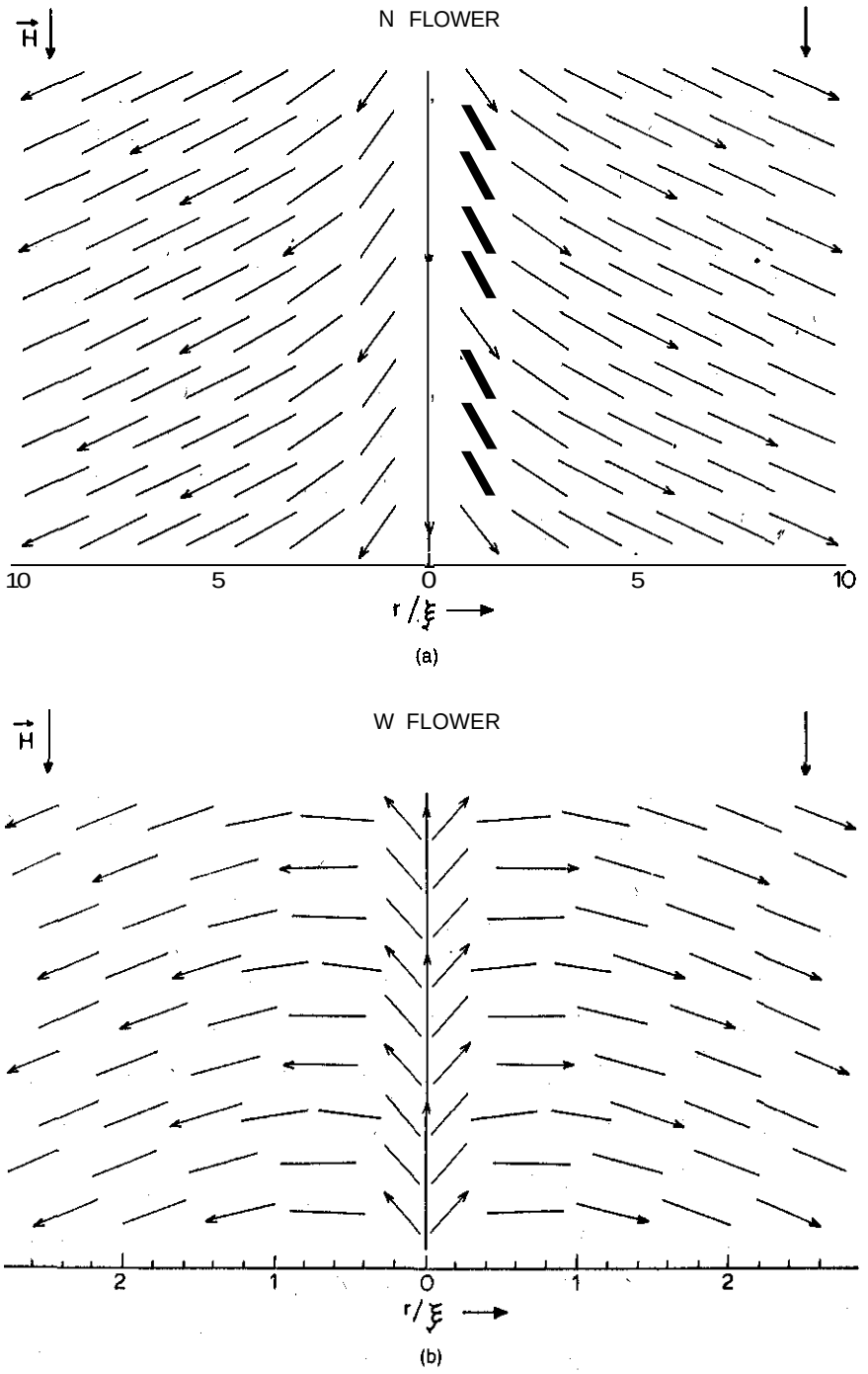

Fig 5.3: (a) N flower and (b) W flower configurations in ferronematics in a magnetic field H = 3000 Gauss.

$$\sin\theta = 0$$

or

$$\text{coso} = \frac{-\text{mf}}{\chi_a H} = \frac{-M}{\chi_a H}$$

When $H < M/\chi_a$, the above condition demands that 0 at $r \to \infty$ to be $2N\pi$. While N = 0 results in a uniform state N $\neq$ 0 leads to the formation of a linear soliton. However, above $H > H_c = M/\chi_a$ the director at $r = \infty$ will be aligned at an angle $\theta_m = \cos^{-1}(-M/\chi_a H)$.

In a field H > H_c it is possible to have two cylindrically symmetric structures as shown in Fig 5.3. One of these structures is rich in splay distortion(Fig 5.3a). It is structurally close to the umbilic obtained for a homeotropicaly aligned nematic with negative diamagnetic anisotropy. The other solution (Fig 5.3b) is rich in bend distortion. These are three dimensional analogues of the 'N' and 'W' walls discussed by Dmitrienko and Belyakov [9] in smectic C* in an electric field. We call them 'N flower' and 'W flower' respectively. just as the N wall is of lower energy compared to the W wall the N flower has lower energy compared to the W flower. However, there is an important difference. The N and W planar solitons (walls) have the same thickness. But we find the thickness of N flower to be much greater than that of W flower. As H $\to$ $H_c$the N flower goes over to the uniform state while the W flower becomes the familiar linear soliton. At the other extreme of H $\to \infty$ both N and W flowers go over to a 'U flower', which has 0 = $\pi/2$ at r $\to \infty$. In fact when magnetic grains are absent,*i.e.*, in pure χ_a negative materials we get only a U flower at every field.

These 'flowers' can exist either in an all radial (bend-splay) configuration ($\varphi = \alpha$) or in an all circular (bend-twist) $\varphi = \alpha + \pi/2$ depending on whether $k_{11}$is smaller or greater than k_{33} .The bend energy is defferent for the two cases. A calculation of energy ignoring grain segregation, gives the interesting result that even when $k_{11} < k_{33}$ a bend-twist configuration can be of lower energy compared to a splay-bend configuration , provided k_{22} is small enough. Likewise, when $k_{11} > k_{33}$ it is possible to have a splay-bend structure to be energetically favorable provided k_{22} is large enough. Grain segregation does not alter very much these results.

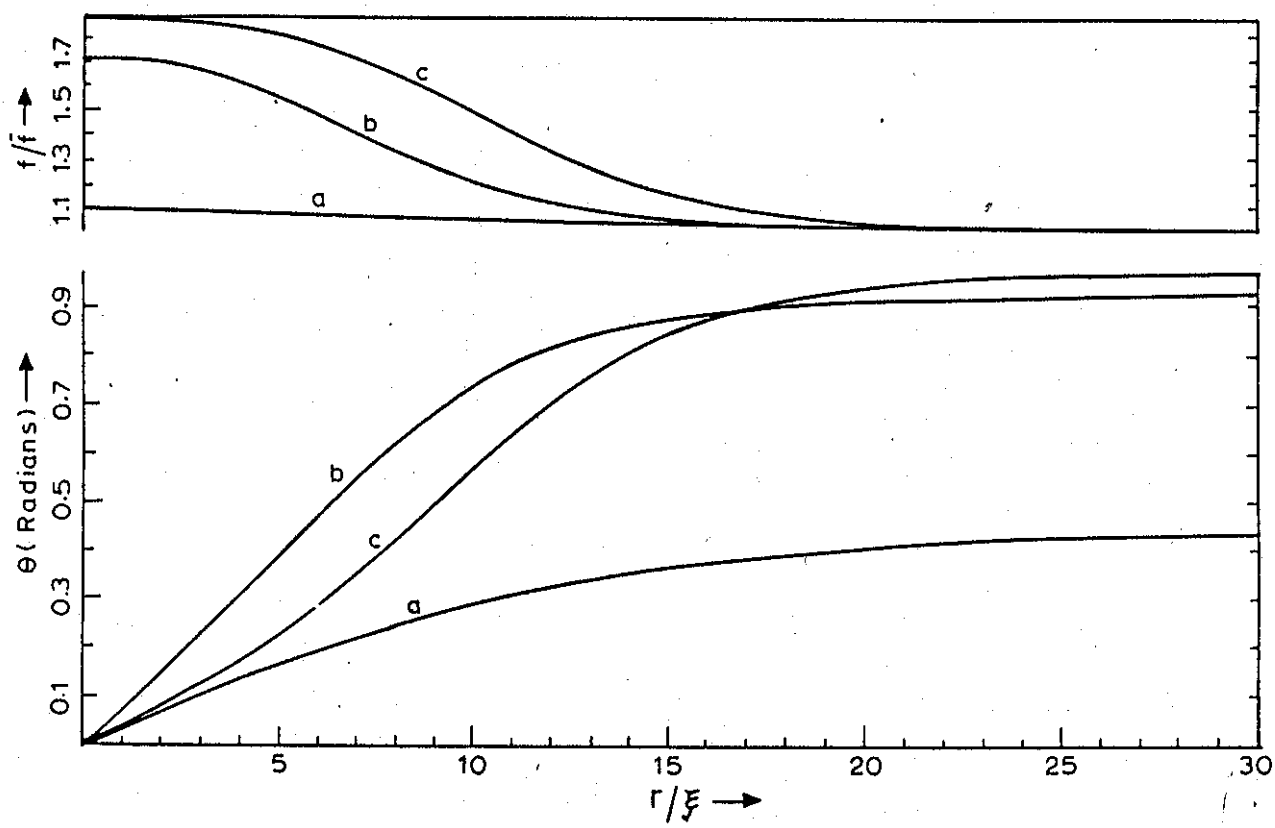

Fig 5.4: The orientation and grain concentration of an N Flower for (a)H = 2000 Gauss, (b)H = 3000Gauss, and (c)H = 3500 Gauss. (H_c = 1800 Gauss).

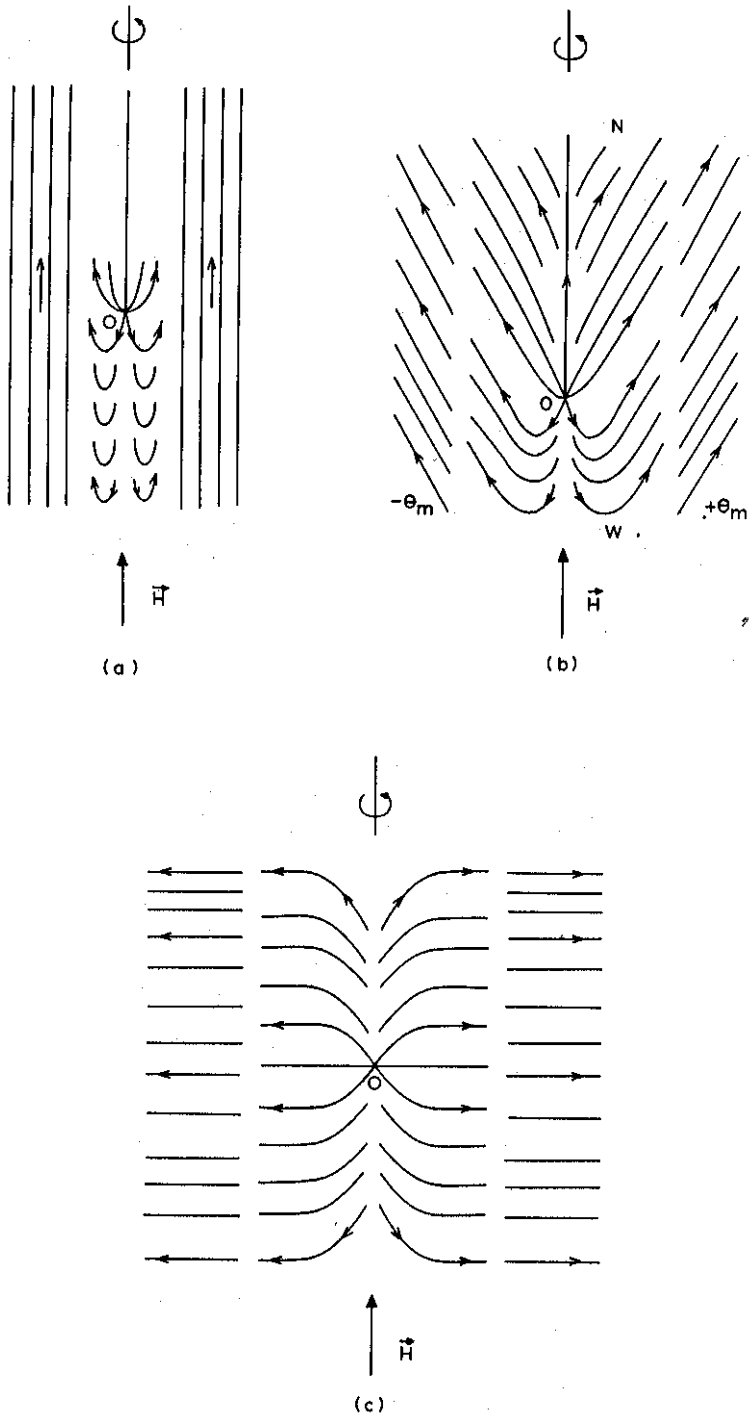

Fig 5.5: Schematic representation of possible transformations of a ferronematic Hedge Hog in a magnetic field. (a) Classical linear soliton for H < H_c (b)N and W Flowers for H > H_c and (c) U Flowers for H $\rightarrow \infty$.

However, the grain segregation does alter the structure and the grain distribution. The minimization of the free energy (5.6) with respect to f leads to a distribution of the grains given by

$$\psi = \frac{f}{\bar{f}} = \exp[\rho_0(\cos\theta - \cos\theta_m)H]$$

We have shown in Fig 5.4 the effect of grain segregation on N flower. As we increase the field above H_c the core thickness decreases in the beginning and later increases. However, the core of W flower is virtually unaltered by segregation over the same range of the field. As the field is increased the grains move out of the core of W flower, while for N flower they move into the core. For higher fields the core of W flower starts shrinking.

Apart from the cylindrically symmetric structures discussed above we can also have structures that lack cylindrical symmetry. For example in the one constant ,approximation we can construct flowers having $\varphi = -\alpha$. They behave like N and W flowers. We call them 'Hyperbolic flowers' as they posses hyperbolic symmetry.

It has already been remarked that the classical Frank energy expression is inadequate to work out the structure and energetics of a linear soliton [6,7]. However,we find, interestingly, that when the orientation at r $= \rightarrow \infty$ is not $\pm\pi$ as in our present case this difficulty does not arise and the problem is completely solvable.

5.2.3 Point defects

It is well known that in a magnetic field a ± 1 point defect of a nematic becomes a linear soliton terminating in the singular point [6,10]. In the case of ferronematics with negative χ_a one expects a splitting of this linear soliton into N flower and W flower solitons above a threshold field. The sequence of possible structural changes with increasing H are shown in Fig 5.5 for a +1 point defect.

5.3 Two component systems

Instead of ferromagnetic grains if we dope a nematic with rod like solute molecules of diamagnetic anisotropy χ_a^s in a nematic host of diamagnetic anisotropy χ_a^h, then a simple extension of the above model permits us, to a good approximation, lo write

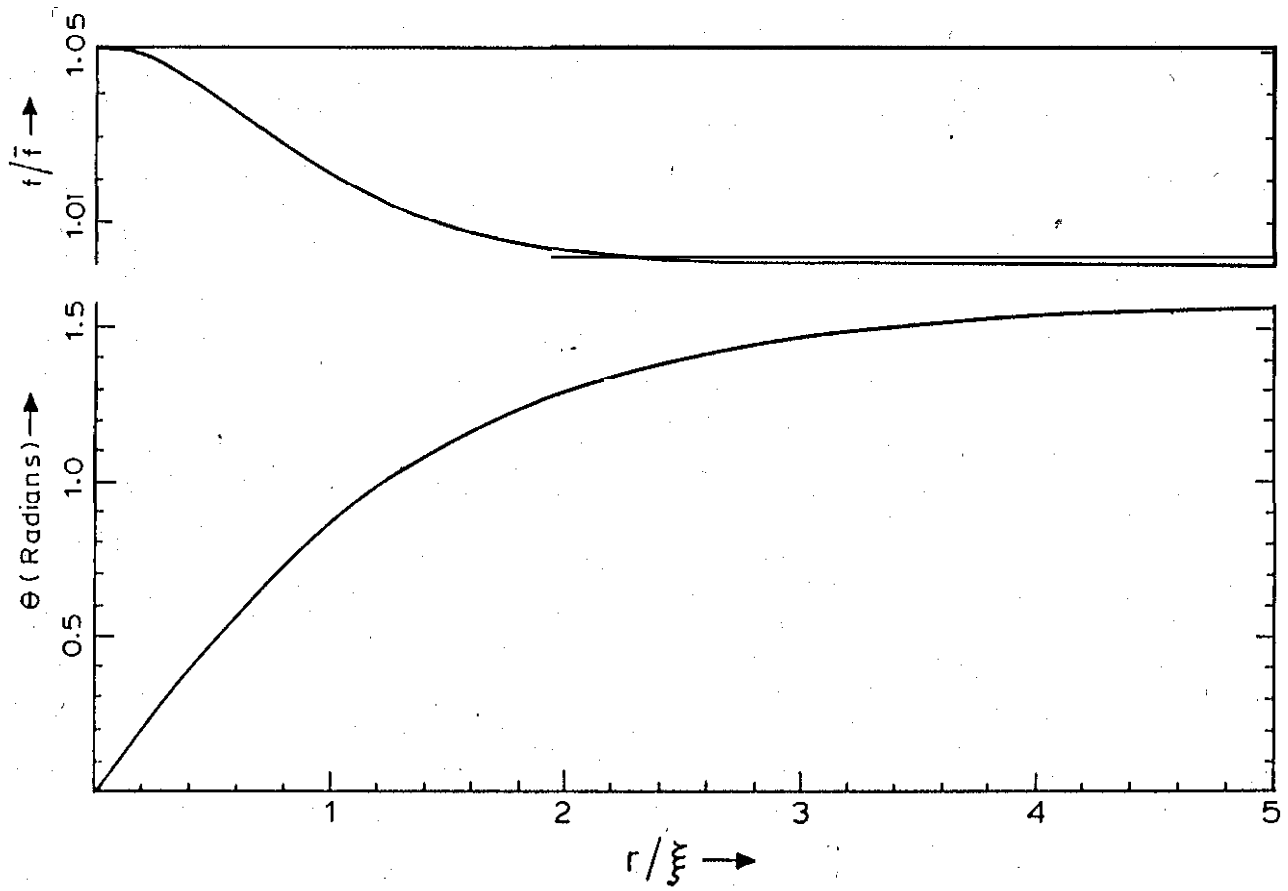

Fig 5 Director tilt θ and grain concentration $f/\bar{f}$ in a nematic with solute molecules. Diamagnetic anisotropy of the solute $\chi_a^s = +10^{-6}$ cgs units and the host $\chi_a^h = -0.5 \times 10^{-6}$ cgs units, $\bar{f} = 10^{-3}$, H = 6000 Gauss, $\rho_0 = 2.0 \times 10^{-9}$ Gauss^{-1}.

the free energy density as follows:

$$F_d = \frac{k}{2}(\nabla\theta)^2 + (\chi_a^h + f\chi_a^s)\frac{h^2}{2}\cos^2\theta + \frac{fk_bT}{V}\ln f.$$

Thus in a magnetic field the solute molecules like the magnetic grains get redistributed in the distorted configuration. In Fig 5.6 is shown this segregation calculated for the U flower configuration with the host and solute molecules having negative and positive diamagnetic anisotropy respectively.

5.4 Ferrocholesterics

We will now work out the structure of ferrocholestrics(FCh) in the presence of magnetic field taking into account the effect of both diamagnetic anisotropy χ_a and the magnetization m of the grains [11]. We will consider both $\chi_a < 0$ and $\chi_a > 0$ materials. We also consider the effects of grain segregation in such structures.

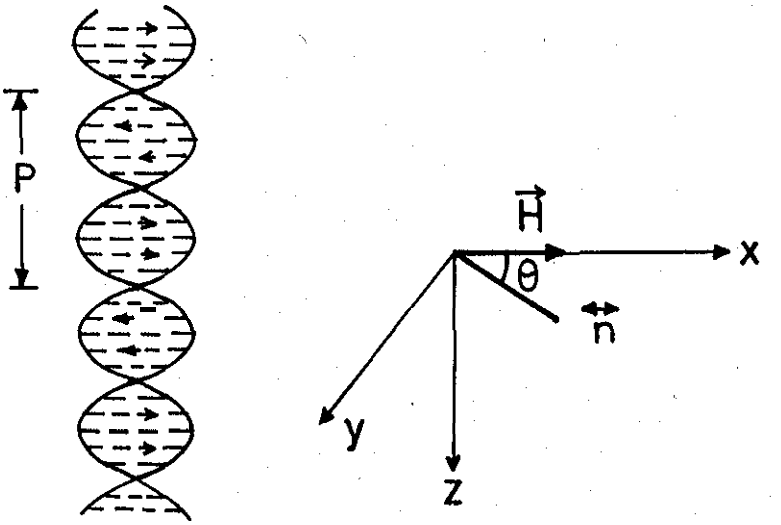

Fig 5.7: Schematic representation of ferrocholesteric in a magnetic field

5.4.1 Elastic instability in ferrocholesterics

As pointed out earlier we incorporate in our analysis the diamagnetic anisotropy of the host matrix. Then the generalized Brochard-de Gennes free energy density of the FCh in a magnetic field (For the geometry shown in Fig 5.7) is given by

$$F_d = \frac{k_{22}}{2}\left(\left(\frac{\partial\theta}{\partial z}\right)^2 - 2q_0\frac{\partial\theta}{\partial z}\right) + \frac{\chi_a H^2}{2}\sin^2\theta - fmH\cos\theta + \frac{fk_BT}{V}\ln f \quad (5.9)$$

where,

k_{22} = twist elastic constant
P = pitch of the FCh = $2\pi/q_0$,

Under the influence of a magnetic field not only the director n gets distorted but also the magnetic grains will get redistributed from their initial uniform distribution. From the minimization of F_d with respect to f, we get,

$$\psi = \psi_0 \exp(\rho_0 H \cos\theta)$$

where, $\rho_0 = (M_s V/k_B T)$ and ψ_0 is the normalization constant so chosen that

$$\int_0^P \psi dz = P \tag{5.10}$$

The Euler equation for θ, is

$$\frac{\partial^2\theta}{\partial z^2} = \frac{\sin\theta\cos\theta}{\xi_1^2} + \frac{\psi\sin\theta}{\xi_2^2} \tag{5.11}$$

where,

$$\xi_1^2 = \frac{k_{22}}{\chi_a H^2} \quad \text{and} \quad \xi_2^2 = \frac{k_{22}}{M_s H \bar{f}} = \frac{k_{22}}{MH}$$

Integrating equation *(5.11)* and using *(5.10)* we get

$$\frac{d\theta}{dz} = \frac{1}{\delta_1}(a - \psi + \delta_2^2 \sin^2\theta)^{1/2} \tag{5.12}$$

where *a* is a constant. Integration of (*5.9)* over one pitch using (*5.12)* leads to:

$$\frac{F}{PMH} = (a-1)\left(\frac{1}{\rho} - \frac{2}{\rho}\right) - \frac{2\pi q_0 \xi_2^2}{P} + \frac{\ln\psi_0}{P} + \frac{\xi_2^2}{P\delta_1}\int_0^{2\pi}\left(a + \delta_2^2\sin^2\theta - \psi\right)^{1/2} d\theta \tag{5.13}$$

The condition for minimum of the free energy $\delta F = 0$ gives,

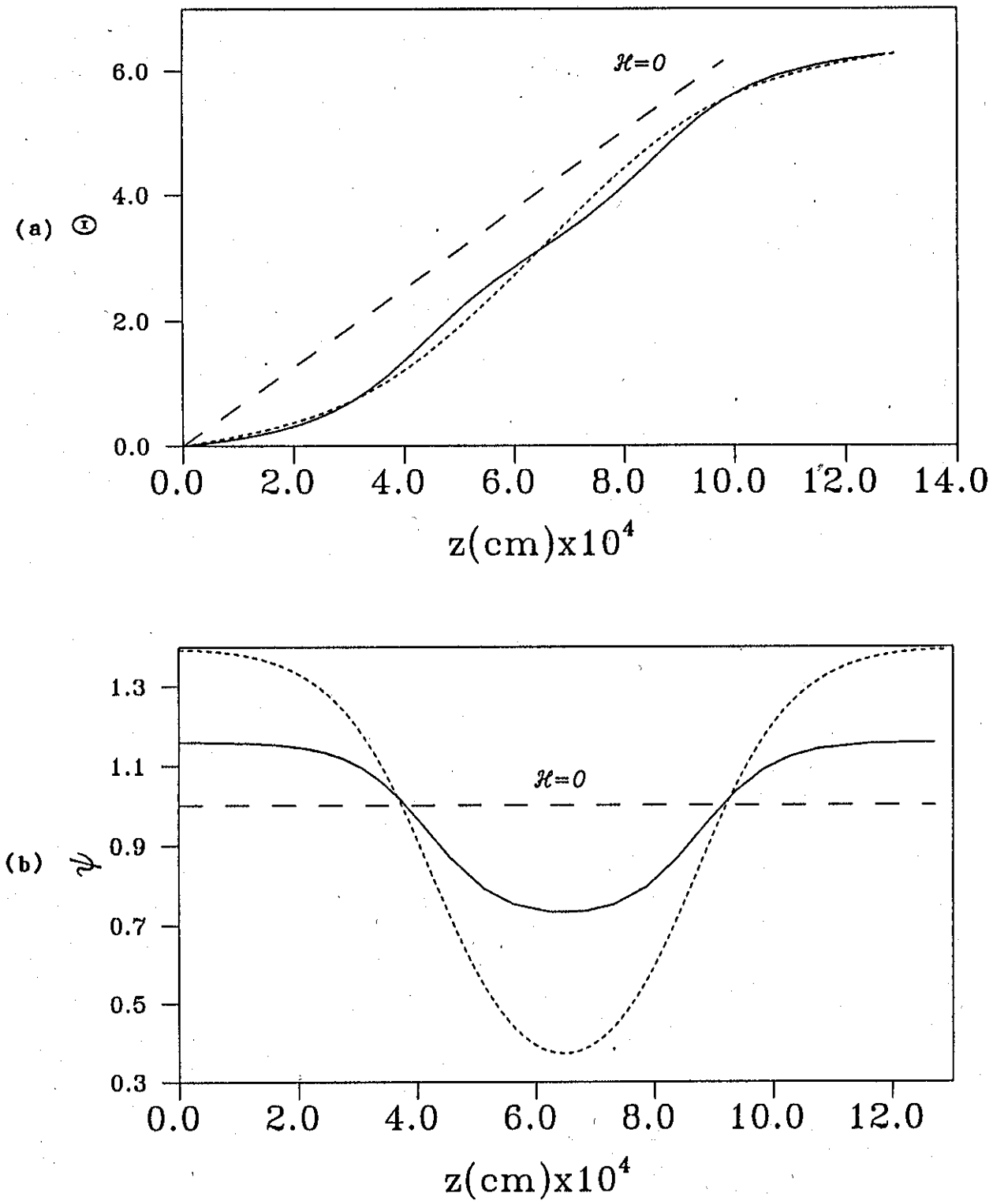

Fig 5.8: The θ profile (a) and ψ profile (b) of a double π lattice shown for one period (continuous line for H > H_c, dashed line for H = 0), for parameters $\chi_a = 5$ x 10^{-6} cgs units, M = 1.8 x 10^{-3} Gauss, H = 7609 Gauss and $\rho_0 = 10^{-4}$. The same for $\chi_a = 0$ is given for (dotted line) for comparison

$$\frac{da}{\rho} + \frac{2\pi q_0 \xi_2^2}{P^2} dP + \frac{1}{\rho}\frac{d\psi_0}{\psi_0} + \frac{\xi_2^2}{2P\delta_1}\int_0^{2\pi}\left(da - \psi\frac{d\psi_0}{\psi_0}\right)\frac{d\theta}{\left(a + \delta_2^2 \sin^2\theta - \psi\right)^{1/2}} - \frac{\xi_2^2}{\delta_1}\frac{dP}{P^2}\int_0^{2\pi}\left(a + \delta_2^2 \sin^2\theta - \psi\right)^{1/2} d\theta = 0 \quad (5.14)$$

From (5.9) and (5.10) we get,

$$\frac{P}{\delta_1} = \int_0^{2\pi}\frac{d\theta}{\left(a + \delta_2^2 \sin^2\theta\,\psi\right)^{1/2}} = \int_0^{2\pi}\frac{\psi d\theta}{\left(a + \delta_2^2 \sin^2\theta\,\psi\right)^{1/2}} \quad (5.15)$$

Substitution of equation (5.15) in (5.14) results in

$$2\pi q_0 \delta_1 = \int_0^{2\pi}(a + \delta_2^2 \sin^2\theta - \psi)^{1/2} d\theta \quad (5.16)$$

here,

$$\delta_1^2 = \frac{\rho_0 H \xi_2^2}{2} \text{ and } \delta_2^2 = \frac{\rho_0 H \xi_2^2}{2\xi_1^2}$$

We can determine ψ_0, a and P by solving equations (5.10), (5.12) and (5.16) simultaneously. These equations have been solved numerically.

5.4.2 Structure of the soliton lattice

For positive diamagnetic anisotropy $\chi_a > 0$ at fields lower than a threshold $H_c = M/\chi_a$ we get, the Brochard-de Gennes 2π soliton lattice - a periodic array of 2π twist walls. However above H_c the 2π lattice becomes unstable with each 2π twist wall splitting into a 'double π' twist wall this has been depicted'in Fig 5.8a (a similar behavior was predicted by Hudák [12] in smecticC^* in an electric field. But we should notice that in smectic C^* there is no process equivalent of grain migration). During the formation of the soliton lattice the grains migrate out of the strongly twisted regions to the weakly twisted regions where the director or m is nearly oriented along the field. Fig 5.8b, shows the grain concentration profile in this case.

For $\chi_a < 0$ materials, the behavior is entirely different. At low fields we get the usual 2π soliton lattice. For fields H $> H_c = M/\chi_a$ the equilibrium orientation of the director in a nematic makes an angle $\theta_m = \cos^{-1}(M/\chi_a H)$ with the field as in

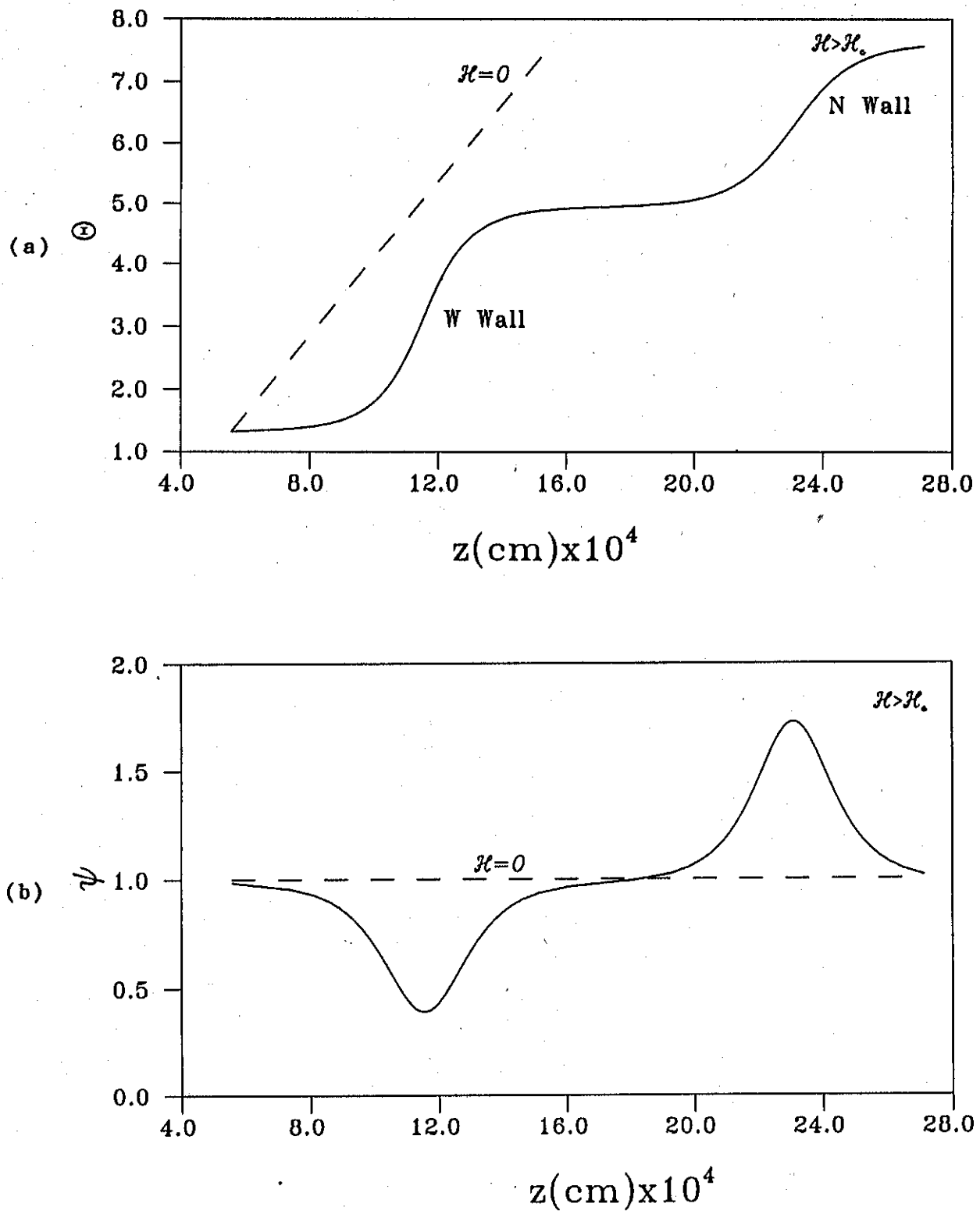

Fig 5.9: The θ profile (a) and ψ profile (b) of N-W lattice shown for one period. $\chi_a = -10^{-6}$ cgs units, $M = 1.8 \times 10^{-3}$ Gauss, H = **22065** Gauss and $\rho_0 = 10^{-4}$.

the case of ferrronematics with negative χ_a. Then each 2π wall splits into a N twist wall and a W twist wall. In the N wall the director turns from $-\theta_m$ to $+\theta_m$ while in the W wall the director rotates from $+\theta_m$ to $2\pi - \theta_m$. It should be remarked that these are very similar to the N and W walls described by and Dmitrienkov and Belyakov for SmC* in an electric field [9] In Fig 5.9a, is shown the θ profile over one period of the N-W soliton lattice. In this case the segregation of magnetic grains has a different profile from that of 2π or double π soliton lattice. This is depicted in Fig 5.9b. It should be noticed that unlike the previous case here the grains migrate from the W wall to the N wall.

Another important difference between the N-W lattice and that of classical 2π lattice pertains to the slope of the twisted regions. In the case' of 2π lattice the twisted region has the same width as the pitch of the cholesteric at $H = 0$. This means that the slope of this region in the $8 - z$ plot is close to q_0. This is no longer true in the N-W lattice. We cart see from Fig 9.a that even though in the N wall the slope more of less close to q_0 in the W wall it is very different from this value. Also the thickness of W wall increases with the magnetization m. However wall thickness is not very sensitive to the grain migration. It can be seen from Fig 5.8a that even in the "double π" wall the two regions have different slopes.

Many of the structural details of cholesteric and ferrocholesteric soliton lattices can be elucidated by an optical technique. This forms the subject matter of the next chapter.

References

[1] Sunil Kumar,P.B., and Ranganath,G.S., 1991, *Mol. Cryst. Liq. Cryst*, 196, 27

[2] Meyer,R.B., 1968, *Appl. Phys. Lett.*, 12, 281

[3] de Gennes,P.G., 1968, *Sol. State Commun., 6*, 163

[4] Brochard,F. and de Gennes,P.G., 1970 *J. Phys. (Paris)*, **31,** 691

[5] Chen,S.H. and Amer,N.M., 1983 *Phys. Rev. Lett*, 51, 2298

[6] Mineev,V.P., 1980, *Soviet scientific Reviews,Section A*, Vol 2

[7] Salomaa,M.M. and Volovik,G.E., 1987, *Rev.Mod.Phys*, 59, 533

[8] Saupe,A., 1973, *Mol. Cryst. Liq. Cryst*, 21, 211

[9] Dmitrienko,V.E and Belyakov,V.E., 1980, *Sov. Phys. JETP.*, 51, 787

[10] Sunil Kumar,P.B., and Ranganath,G.S., 1989, *Mol. Cryst. Liq. Cryst*, 177, 123

[11] Sunil Kumar,P.B., and Ranganath,G.S., Structure and optical properties of cholesteric soliton lattices, *J.Physics (paris)-II* — to appear in October 1993

[12] Hudák,O., 1983, *J. Physique (Paris), 44*, 57